Defect and Diffusion Forum *Online: 2011-03-15*
ISSN: 1662-9507, Vol. 311, pp 62-104
doi:10.4028/www.scientific.net/DDF.311.62

Impurity Centers in Oxides Investigated by γ-γ Perturbed Angular Correlation Spectroscopy and *ab initio* calculations

Alberto F. Pasquevich[a] and Mario Rentería[b].

Departamento de Física and Instituto de Física La Plata (IFLP, CCT La Plata, CONICET), Facultad de Ciencias Exactas, Universidad Nacional de La Plata, CC 67, 1900 La Plata, Argentina.

[a] pasquevi@fisica.unlp.edu.ar, [b] renteria@fisica.unlp.edu.ar

Keywords: semiconductors - defects - diluted magnetic oxides - trapped holes - indium oxide - hafnium oxide - binary oxides - titanium oxide

Abstract. In this chapter Perturbed Angular Correlation (PAC) experiments on binary oxides are described. These experiments provide local-scale fingerprints about the formation, identification, and lattice environment of defect complexes at the PAC probe site. The potential of the PAC observations in conjunction with *ab initio* calculations is shown. Measurements of the electric-field gradient at impurity sites using ^{111}Cd and ^{181}Ta probes are reviewed. Special attention is paid to oxides with the bixbyite structure. The case of In_2O_3 is particularly analyzed. Results obtained with HfO_2, in form of coarse grain or nano particles, are described. The potential results that can be obtained from Density Functional Theory *ab initio* calculations in doped systems are shown describing the main results observed in many impurity-host systems.

Introduction

During the last two decades, the Time-Differential Perturbed-Angular-Correlation (PAC) technique has been extensively applied to the characterization of all kinds of materials. In particular, the work done on binary oxides has been very complete.
In all the cases, the nuclear sensitive state of the probe-atom necessary in this spectroscopy appears in the host material following the disintegration or decay of a parent isotope. Hence, the probe-atom will be the daughter of either an isobaric or isomeric isotope. In general, the probe-atom will be a very dilute impurity in the oxide under study.
It is necessary to deal with "impurity centers" in almost every PAC determination. In general, it is from an impurity center that the probe atomic environment is characterized. Due to this fact, the question concerning at what extent the probe-atom is a "good observer" of the structural and electronic properties of the material or those of the new impurity-host system becomes relevant.
On the other hand, impurities are important defects in a wide range of materials since many of their macroscopic properties depend on the type and concentration of these defects. In the specific case of the oxides, the technological applications of many of them depend on the modified properties introduced by the impurities. In this sense the PAC technique, having its tracers located at the "eye of the storm", can supply unique and valuable information about the impurity center configuration and the properties of the doped systems.
In this chapter a review of the PAC studies performed on binary oxides using ^{111}Cd and ^{181}Ta impurities as probe–atoms is given. Results of selected experiments that have given by themselves important information are described, as well as cases in which *ab initio* calculations were necessary to explain more complicated scenarios. In addition, through selected examples a revision of all the structural and electronic properties that can be obtained about an impurity-host system from a combined experimental-*ab initio* approach is done: structural relaxations, charge state of the impurity center, character of the impurity level, total and partial density of states per atom and per

orbital, symmetry of the valence electronic charge density and that of the impurity level, orbital contributions to the electric-field gradient, and its sign and orientation.
After many years of application there is still the expectation that PAC experiments in oxides will uncover interesting physics [1]. Indeed, in oxides, there are fields where the PAC technique has still to contribute. These are the cases, e.g., of Dilute Magnetic Semiconductors (DMS) and of trapped holes at impurity centers. Both fields are reviewed. In the case of the ^{111}Cd probe, its apparition in the host is accompanied with the production of several holes at the center. The presence of these holes and their recombination with electrons give place to fast fluctuations in the hyperfine interactions sensed by the probe. This effect is also reviewed together with some models used for its description.

Metal oxides

The oxides of metals exhibit a wide range of electrical, optical, magnetic, and chemical characteristics. A useful classification of these interesting solids can be made into "closed shell" oxides which may be considered to be formed from oxygen ions O^{2-} and metal ions with a filled electronic shell and oxides of the transition -, lanthanum- , and actinium-series of metals for which the constituent metal ions do not have a complete electronic shell.
The energy band theory of the solids, which has been rather successful in the explanation of the properties of metals and covalent crystals such as silicon and germanium, appears to be applicable to metal oxides, although a complete interpretation of the properties of dilute metal oxides by band theory has yet to be made.
The magnitude of the energy gap between the uppermost filled band (oxygen 2*p*) and the lowest empty band of oxides, E_g, depends sharply on the type of metal forming the oxide. Available values of the E_g for closed shell metal oxides indicate that E_g decreases sharply with the decrease of the electronegativity difference $\Delta\chi$ between the metal and the oxygen. E_g also decreases with the value of the principal quantum number n of the valence electrons of the free neutral metal atoms.
Although the oxides have different crystal structures and hence differ in energy band structure, the dependence of E_g on $\Delta\chi$ parallels the increase in covalent character of the corresponding metal – oxygen bonds with decrease in $\Delta\chi$.
Closed shell metal oxides may thus be subdivided into insulators such as MgO and Al_2O_3 and semiconductors such as ZnO or In_2O_3. Oxides of metals of the first transition series behave as insulators, semiconductors, and in some cases as metals, due to the presence of the incomplete 3*d*-shell.

Impurity centers in oxides. Trapped holes and bound polarons

Valence band holes in oxide materials tend to be trapped at negatively charged acceptor defects. Schirmer [2] reviewed these defects, described as small polarons bound to an acceptor.
Examples are provided by transition metal or rare earth ions with lower valences than the replaced cations, but also cation vacancies and simple ions, such as Li^+, Mg^{2+}, Al^{3+},etc. In the latter cases, the electron ionization energies are high and a hole will thus be captured at the neighboring oxygen ions rather than at the defect itself. In crystalline solids there are usually several equivalent oxygen sites surrounding a point defect. Cases of tetrahedral symmetry, with four equivalent oxygen sites, and with octahedral symmetry, comprising either six or twelve equivalent sites, have been investigated. In spite of the equivalence of the oxygen ions in such clusters, in most cases it turns out that hole–lattice coupling favors hole localization at a single one among them, forming an isolated O^- ion. This is caused by lattice distortion, breaking the point group symmetry. It is thus useful to label such defects as small polarons, bound to an acceptor. For small polarons the carrier is essentially restricted to one site and the distortion mainly involves the bonds to its first neighbors.

The lattice distortion stabilizing a polaron is counteracted by tunneling, which is facilitated by the equivalence of the sites concerned. The tunneling leads to nearly degenerate Bloch states and lattice interaction has to deal with the corresponding lack of degeneracy. For the ground states of strongly localized polarons, however, tunneling is only a small but decisive perturbation.
It turns out that these simple systems, single O^- ions next to acceptor defects in oxide systems, have a series of intriguing aspects, as regards their electronic and ionic structure as well as their optical features, the methods of their investigation and their roles in various applications of oxide materials. The holes to be trapped at acceptor defects are created by chemical or optical doping. The latter procedure is used predominantly. Usually electrons are excited from the valence to the conduction band or to defects having levels in the gap, forming valence band holes. Less frequently also a direct optical ionization of O^{2-} ions next to an acceptor to the conduction band takes place. These excitation processes can be caused by the absorption of photons or the secondary radiation effects following x-ray, electron or neutron irradiation. The electron-capture (EC) decay of radioactive impurities (like ^{111}In (EC) ^{111}Cd) produces several holes at the impurity center. Since the created situations represent deviations from the crystal ground states, they are not stable and eventually the holes will recombine with the electrons separated from them. Such electrons are often accommodated at levels near to the conduction band edge. The lifetime of the hole states, with which we are concerned, is determined by the shallower of the two species, trapped electron or hole. In wide band-gap materials, such as quartz, the hole lifetimes can still be effectively infinite at room temperature as exemplified by holes next to Al^{3+}, caused by the radioactivity at the geological deposit of quartz. The O^- next to Al^{3+} can be at least partly responsible for the smoky coloration of quartz [2]. A strong chemical doping with acceptor defects can lead to spontaneous compensation by holes, without further illumination. In such a case, the Fermi level is stabilized at the acceptor level and partially filled acceptor states occur. Sometimes, however, an additional heat treatment in an oxygen atmosphere is necessary for removing competing intrinsic positive defects, such as oxygen vacancies, in order to achieve this situation. This is known to take place, e.g., for Al_2O_3 doped with Mg [3], and the hole-concentration increases strongly with rising oxygen partial pressure.
In crystalline quartz two O^--type defects are known, O^- next to Al^{3+} [4] or to Ge^{4+} [5], which show absorption bands typical for bound hole polarons. Al^{3+} is charged negatively with respect to the replaced Si^{4+} and can thus stabilize a hole at a neighboring oxygen ion by Coulomb attraction. Germanium is amphoteric in quartz, i.e. Ge^{4+} can trap an electron as well as a hole [5]. In the two cases the electronic structures of the O^- defects are similar: the ground state 2*p* lobe is oriented perpendicular to the plane spanned by Al (Ge), O^- and Si^{4+} (see Fig. 1).

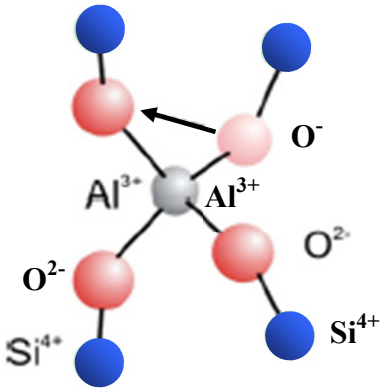

Fig. 1: Section of quartz crystal (as viewed along the c-axis) around Al^{+3} (or Ge^{+4}) defect on a Si^{+4} site. A hole has been captured at one of the neighboring O^{2-} ions. Among the possible charge paths, one is symbolized by the arrow. Recreated from Ref. [2].

Experimental techniques applied to the study of trapping of holes at impurity centers in oxides.

On the experimental side, numerous methods have been used to elucidate the properties of the O^- systems. For crystals with non-magnetic host lattice cations, basic knowledge on their electronic and geometric structure always results from studies of electron paramagnetic resonance (EPR), augmented by optically detected magnetic resonance (ODMR) and the study of light-induced optical absorption changes.
O^- ions next to acceptor sites have rather unique magnetic fingerprints, allowing one to prove their presence as well as to identify the underlying microscopic structure of the related defects by using several electron resonance techniques, at least in crystals with non-magnetic cations. An O^- ion is paramagnetic, since one electron is missing in the oxygen 2*p* shell. In the non-cubic environments of such ions, either present in the unperturbed crystal already or caused by association with defects together with the accompanying lattice distortion, the coupling of the S = 1/2 spin to the 2*p* orbital (L = 1) is weak in most cases, leading to rather long spin–lattice relaxation times. Zeeman interaction with an external static magnetic field, B, and hyperfine coupling with magnetic nuclei within the range of finite hole amplitudes determine the structure of the spectra of such O^- systems. These centers can be studied and monitored by the powerful magnetic resonance techniques [mainly electron paramagnetic resonance EPR [6], but also electron nuclear double resonance (ENDOR) [7] and optically detected magnetic resonances ODMR [8-9]. For applications to absorption signals, the magnetic circular dichroism (MCD) occurring in a static magnetic field is exploited [9].
The PAC technique applied to determine the Electric-Field-Gradient (EFG) tensor at the site of the probe-atom ^{111}Cd in closed-shell metal oxides gives evidence of the interaction with holes, produced by the EC-decay of ^{111}In, with the Cd acceptor impurity. Effects associated with these holes, have been observed, for example, in In_2O_3 [10, 11], Al_2O_3 [12], La_2O_3 [13], Ga_2O_3 [14], SnO_2 [15], SnO [16], Lu_2O_3 [17,18], Cr_2O_3 [19], etc. Among these examples in which their PAC spectra show time-dependent hyperfine interactions, we will find those that can be described by a unidirectional electronic relaxation (as in the first six cases) and those described by a fast fluctuation between two electronic states (the last two cases) of the impurity. The first class of interaction will be described in detail in another section.

Theoretical calculations of physical properties of impurities centers in oxides.

Impurities introduce structural distortions in the host lattice and can modify the distribution of charge in its neighborhood. For these reasons it is more appropriate to call such a defect *impurity center*. One way to measure electronic properties on an atomic scale is to use hyperfine experimental techniques. In particular, PAC provides a high-resolution determination of the EFG tensor at the site of the probe atom, a quantity particularly sensitive to slight local changes in the electronic charge density around the impurity- probe. The measured EFG may give structural and electronic information of the system that cannot be obtained by other methods, but the interpretation of such measurements is not straightforward. In fact, interpretation of experimental EFG results involves understanding of chemical differences between the probe atom and the ion replaced by the impurity. The experimental results show that the differences between probes and indigenous atoms are manifested many times in subtle ways that are not well described by simple models, as already pointed out by Adams *et al*. [20]. Local and very precise information about the system under study, provided by the EFG tensor, can be obtained by comparing experimental results with an accurate calculation of the EFG tensor [21]. In the case of doped systems, for an accurate calculation of the EFG, the electronic configuration of the host, perturbed by the presence of the impurity, has to be determined. This can be done in the framework of the density-functional theory (DFT) [22]. In this kind of calculation, electronic and structural effects introduced in the host by the presence of the impurity probe (impurity levels, structural distortions, etc.) can be described without the use of arbitrary suppositions. For such purposes, DFT calculations using the full-potential augmented

plane wave plus local orbitals (FP-APW+lo) method [23, 24] have been performed in different type of doped materials (semiconductors [25], oxides [26,27], and intermetallics [28]). A detailed description of the methodology employed in these calculations to deal with the complexity of the impurity-host system is given in Ref. [27] and an extensive discussion of the results restricted to doped oxides can be found in Errico *et al.* [29] and Darriba *et al.* [30]. In all calculated cases, the amount of structural distortion per atom decreases rapidly from the impurity nearest oxygen neighbors to the other shells. ^{111}Cd, e.g., on both In-sites of In_2O_3 causes relaxations of about 5% of the nearest oxygen neighbors of the Cd impurity. [31, 32]. Larger relaxations (even anisotropic) were found in TiO_2 [26,27] and SnO_2 [33]. It was concluded that the Cd impurity tries to reconstruct the environment of Cd in its own oxide [29,30]. The excellent agreement between the *ab initio* calculations and the PAC experiments with the ^{181}Ta probe stabilize this interpretation [30,34-37]. In these cases, contractions or relaxations are observed if the Ta-O distance in TaO_2 is shorter or larger than the cation-oxygen bond-lengths in the studied oxides.

As we already pointed out, the experimental evidence for cation-site acceptors in wide gap oxides demonstrates that holes often lock into individual oxygen ligands instead of being distributed over all symmetry-equivalent oxygen sites, e.g., in the case of Al in SiO_2 or Li in ZnO [2,38-40]. Formally, the hole binding can be described by the change in the oxidation state of individual O atoms from the normal O^{2-} into an O^- state. A systematically consistent theoretical description of such acceptor states remains, however, challenging as common DFT calculations in the local density approximation (LDA) or generalized gradient approximation (GGA) fail to reveal the correct hole localization on just one O atom and the associated lattice relaxation effects. This failure has been traced back to a residual self-interaction present within the oxygen *p* shell in LDA or GGA [41-44]. Hartree-Fock theory, on the other hand, is known to overestimate the tendency toward hole localization on individual lattice sites [40]. The correct description of the balance between competing tendencies toward single-site localization vs. delocalization among equivalent sites bears great importance for physical phenomena such as hyperfine interactions [43], d_0 ferromagnetism [44-47] and *p*-type doping in wide-gap oxides [48]. Lany *et al*. applied this method to quantitatively predict the acceptor transition energies for the cation-site acceptors in ZnO, In_2O_3, and SnO_2 [49]. In all cases studied, they find that these acceptors introduce states at rather deep energies inside the band gap and can bind even multiple holes despite the fact that from their position in the periodic table they are expected to be single acceptors.

Dilute Magnetic Semiconductors

Ferromagnetism (FM) in undoped non-magnetic oxide materials like CeO_2, ZnO, In_2O_3, SnO_2, Al_2O_3, etc., remains a controversial issue till date. Doping of ferromagnetic and non- ferromagnetic elements like Mn, Co, Fe, Cr, Cu, etc., in such oxides have yielded a significant amount of ferromagnetism at room temperature and various exchange mechanisms like superexchange, Ruderman-Kittel-Kasuya-Yosida (RKKY) exchange have been proposed for explaining the ferromagnetism in doped oxide materials. In the case of undoped oxides, the origin of ferromagnetism is also still a matter of active research. This ferromagnetism was first reported in 2004 for thin films of hafnium dioxide (HfO_2) dielectrics grown using pulsed laser deposition on saphire or silicon substrates [50]. Since the nominal valence of Hf in HfO_2 is 4+, which leaves Hf atoms with an empty *d*-shell, the phenomenon was initially termed *d_0 ferromagnetism*. This phenomenon is of paramount interest to properly understand the origin of DMS using oxide materials. The mentioned films had a Curie temperature exceeding 500 K and a magnetic moment of about $0.15\mu_B$ per HfO_2 formula unit. The magnetization was anisotropic.

Ab initio electronic structure calculations using DFT in HfO_2 have shown that isolated hafnium vacancies lead to ferromagnetism [51]. At the same time similar studies [52] performed in pure rutile TiO_2 with one oxygen vacancy in a 12-atoms supercell give two possible degenerate solutions, one nonmagnetic and the other having a magnetic moment of approximately $1\mu_B$ per vacancy, due to polarization of the Ti atoms. It is worth mentioning that the magnetic phase

appeared only when the structural relaxation was taken into account. This unexpected result anticipated that a large concentration of oxygen vacancies could play an important role in the magnetic behavior of doped rutile TiO_2 but also in oxygen deficient TiO_2. Lower concentrations of oxygen vacancies predicted smaller magnetic moment for the rutile structure and none for the anatase structure. It seems that the appearance of a magnetic moment may depend on the vacancy concentration in the oxide and on the structure. Subsequently to these studies, ferromagnetism was observed in TiO_2 and In_2O_3 thin films [53]. Following the theoretical studies of Ref. [52], Weissmann *et al.* [54] found that the magnetism in reduced TiO_2 depends on the vacancy concentration and on the strain of the structure, produced either by the substrate or by the growth procedure of the films. It is worthy of mention that the differences in the spin densities obtained in these studies [52,54] adding magnetic and non-magnetic impurities, such as Co and Cu, and changing the crystal structure (rutile and anatase), raised the question if the mechanism for long range ferromagnetic order is the same for both types of doping, and also if it is the same for undoped films.

In the case of In_2O_3 thin films it was further observed that the ferromagnetism depends on the substrate and the direction of the magnetic field. In_2O_3 films on MgO showed isotropic ferromagnetism at room temperature whereas In_2O_3 films on Al_2O_3 substrates exhibited diamagnetic behavior for magnetic field parallel to the film and ferromagnetic behavior for perpendicular magnetic field. It is to be noted that the bulk of the oxide materials described above were diamagnetic. However, the nanoparticles of these materials have been shown to be ferromagnetic in nature [55].

So far there has been no unified theory for explaining ferromagnetism in all oxide materials. A model based on an electronic structure calculation using the tight-binding method in the confinement configuration proposes that the vacancy sites in TiO_2, HfO_2 and In_2O_3 films could create spin splitting and high spin states, so that the exchange interaction between the electrons surrounding the oxygen vacancy with the local field of symmetry could lead to a ferromagnetic ground state of the systems [56].The calculations provided the following results: 3.18 μ_B per vacancy for TiO_2, 3.05μ_B per vacancy for HfO_2 and 0.16μ_B per vacancy for In_2O_3. This model suggests that the mechanism for ferromagnetism in ZnO system must be different and cannot originate from oxygen vacancies but from other sources. Very recently a model on the d_0 ferromagnetism for a ZnO model system suggested that a generalized hole-induced magnetization in oxides, nitrides and diamond is an intrinsic host property when enough homogeneous holes are injected into the system [57]. It was further demonstrated that localization of the holes by dopants and quantum confinement effect can reduce the critical hole concentration for stabilizing the magnetization. The non-monotonic spin coupling in this system is explained by considering band broadening as a function of defect–defect separation. Ferromagnetism has also been reported in pristine SnO_2 [58]. From the above discussion the presently unresolved status of the research on ferromagnetism in undoped oxide systems, especially In_2O_3 and SnO_2 systems in the context of this chapter, is obvious. It can be safely said that the origin of ferromagnetism in such materials is predominantly induced by structural defects. The effect of the oxygen vacancies was investigated in the annealing experiment performed by Hong *et al*. [58], where oxygen annealing of films showed a drastic decrease in the ferromagnetic behavior, while their prolonged storage (i.e., oxygen loss from the surface) led to the re-emergence of the ferromagnetism. This effect had been reported previously by Duhalde *et al.* [59] in TiO_2 thin films growth by PLD on $LaAlO_3$ substrate, doped with Cu, in which unexpected significant RT ferromagnetism was observed although Cu is a nonmagnetic impurity. *Ab initio* calculations performed in this case showed that the presence of Cu lowers the energy formation of oxygen vacancies, essentials for the appearance of the ferromagnetism. Once again, a thermal annealing in oxygen-rich atmosphere for some minutes produced a drastic reduction of the magnetic signal, in agreement with the *ab initio* predictions [59]. Recently, Majundar *et al*. have reported room temperature ferromagnetism in indium tin-oxide commercial electrodes [60].

Time dependent hyperfine interactions.

As was already described in chapter one, in a PAC experiment the perturbation of the angular correlation of two consecutive nuclear γ -rays is determined by the hyperfine interaction of the intermediate nuclear level with its electric environment (for simplicity we will not considerer cases of magnetic interactions here). The Fourier transform of a static PAC spectrum consists, in general, of triplets of sharp frequencies (in the case of I=5/2 and $\eta < 1$) related with a certain EFG acting in an ensemble of probe nuclei (e.g., at a particular crystallographic site). A *static* damping of the PAC time spectrum occurs if different nuclei sense slightly different static EFGs due to distortions in their remote neighborhood. In a dynamic description, the environment of an individual nucleus changes during the lifetime of the sensitive level leading to *dynamic* damping and phase shifts in the spectrum. Winkler and Gerdau developed a description of PAC spectra for dynamic hyperfine interactions based on stochastic processes [61]: the environment of a probe nucleus may instantaneously change between different environmental states. This theory has been applied to fluctuating EFG's originating from the trapping and release of charges [17-19,62]. In these cases the charge carriers were in thermal equilibrium with their environment.
A different situation which is of special interest in this chapter arises in connection with the decay of the parent of the PAC probe: the decay could leave the probe ion in a highly charged state far out of equilibrium. These electronic "*after-effects*" (AE) can occur, for example, in the case of K-electron-capture decay: an electronic hole is produced in the K shell, this hole is filled up with an electron of outer shells within a very short time [63], much too fast to have any influence on the PAC spectra. But, at the same time, the probe ion loses quite a large number of electrons due to Auger processes. Highly charged states of ions in a solid become compensated by electrons from their next-neighbor ions within less than about 10^{-12}s. Only ions with one or two extra (*positive*) charges with respect to their appropriate charge state in the solid then may remain stable for times long enough to reach the sensitive time scale (given by the half-life of the intermediate level of the γ - γ cascade). In this ''time-window of the measurement'' transitions still occur to the final stable probe charge state. In this case, the electronic configuration of the nearest oxygen neighbors of the probe-atom change and the nucleus feels fluctuating EFGs. As we already mention, effects of this type, have been observed, for example, in In_2O_3 [10, 11], Y_2O_3 [64], Sc_2O_3 [64], Al_2O_3 [12], La_2O_3 [13], SnO_2 [15], Ga_2O_3 [14], and SnO [16] when doped with ^{111}In. All these oxides are closed shell oxides, insulators or semiconductors. On the other hand, oxides of metals of the transition series do not present the effect due to the presence of the incomplete *d*-shell, which servers as an electron buffer. We will be back on this topic in the description of the PAC measurements in In_2O_3. Here we review some models developed to deal with the existence of electronic AE following a K-electron capture, internal conversion or β-decay.
To show how the AE appear in the PAC results, in Fig. 2 we reproduce PAC spectra of La_2O_3:^{111}In taken at different temperatures [13].
The physical situation was simulated with the program DYNXWW [65] developed by Lupascu. The code was conceived to calculate any dynamic perturbation function based on the model of Winkler and Gerdau [61], and in a latter refinement developed by Achtziger and Witthuhn [62]. With the Lupascu´s code [13,66] numerical solutions can be obtained for a set of initial states V_{ij} of arbitrarily chosen asymmetries and orientations in space and dynamic transitions between them. A stable final configuration is reached with a relaxation rate λ_r and characterized by $V_{ij}(f)$. In this case of unidirectional relaxation, the calculated spectra (see Fig. 3) show the characteristic behavior of Fig. 2: All the phase shifts vanish if fluctuations between the initial states are allowed. Lupascu *et al*. introduced the relative amplitude of $V_{ij}(f)$, as $r = f_{obs} / f_{max}$ where f_{max} denotes the maximum fraction found in static cases. r depends on the total relaxation rate λ_r populating $V_{ij}(f)$.
As we see, the Lupascu´s description reproduces very well the experimental results between room and high temperatures: the fluctuations of EFG´s (in the limit of very fast fluctuations) produce a fast lost of the R(t) - anisotropy, without any change in frequency.

Unfortunately, the numerical calculation used by Lupascu *et al*. makes the fitting of the experimental data difficult. In this sense it is better to go back to the old proposal of Bäverstam *et al*. [67]. This model has the advantage that leads to an analytical expression for the perturbation factor. At that time several calculations of the perturbation factors in time-dependent interactions had been published [68-72] but none of them is however directly applicable in the case presently discussed. Let us see the Bäverstam *et al.* model:
The most general expression for $G_{22}(t)$ may be written:

$$G_{22}(t) = \sum_i c_i \exp(a_i t)$$

where c_i and a_i may be complex numbers. If the following conditions are satisfied:

(i) the correlation time τ_c, which is a typical time for the changes of the nuclear environments, is small enough to let $\omega\tau_c << 1$, where ω is the nuclear precession frequency;
(ii) the time of observation $t >> \tau_c$;
(iii) the interaction is so small that the first-order perturbation theory is valid; then the same result will be obtained by all theories:

$$G_{22}(t) = \exp(-\lambda_r t)$$

λ_r is called the relaxation constant. In this case atomic recombination and electronic de-excitation time constants are included in λ_r. These processes have very short correlation times. Thus conditions (i) and (ii) seem to be fulfilled. If the interaction is stronger than what is assumed in (iii) $G_{22}(t)$ will be , according to the Dillenburg and Maris theory [69], the sum of two exponentials. The nuclei of the excited atoms are feeling a static field besides the time dependent interaction. Since the static interaction is much weaker than the time-dependent one, $G_{22}(t)$ can be expressed, for the combined static and time-dependent interactions, as the product:

$$G_{22}(t) = G_{22}^s(t) \exp(-\lambda_r t) \quad , \qquad [1]$$

where $G_{22}^s(t)$ represents the perturbation due to the static field.
The fact that the excited atoms, after a certain time, will reach their electronic ground states had not yet been accounted for. To do this, two simplifying assumptions were made:
(i) That the probability for an atom reaching its ground electronic state after the time t' is:

$$P_g(t') = \lambda_g N \exp(-\lambda_g t'),$$

where N is the number of probes that will contribute to G_{22} at time t and λ_g is the probability per unit of time for an atom to reach the electronic ground state.
(ii) That the mean interaction strength averaged over all excited atoms is constant, i.e., λ_r is still a constant.

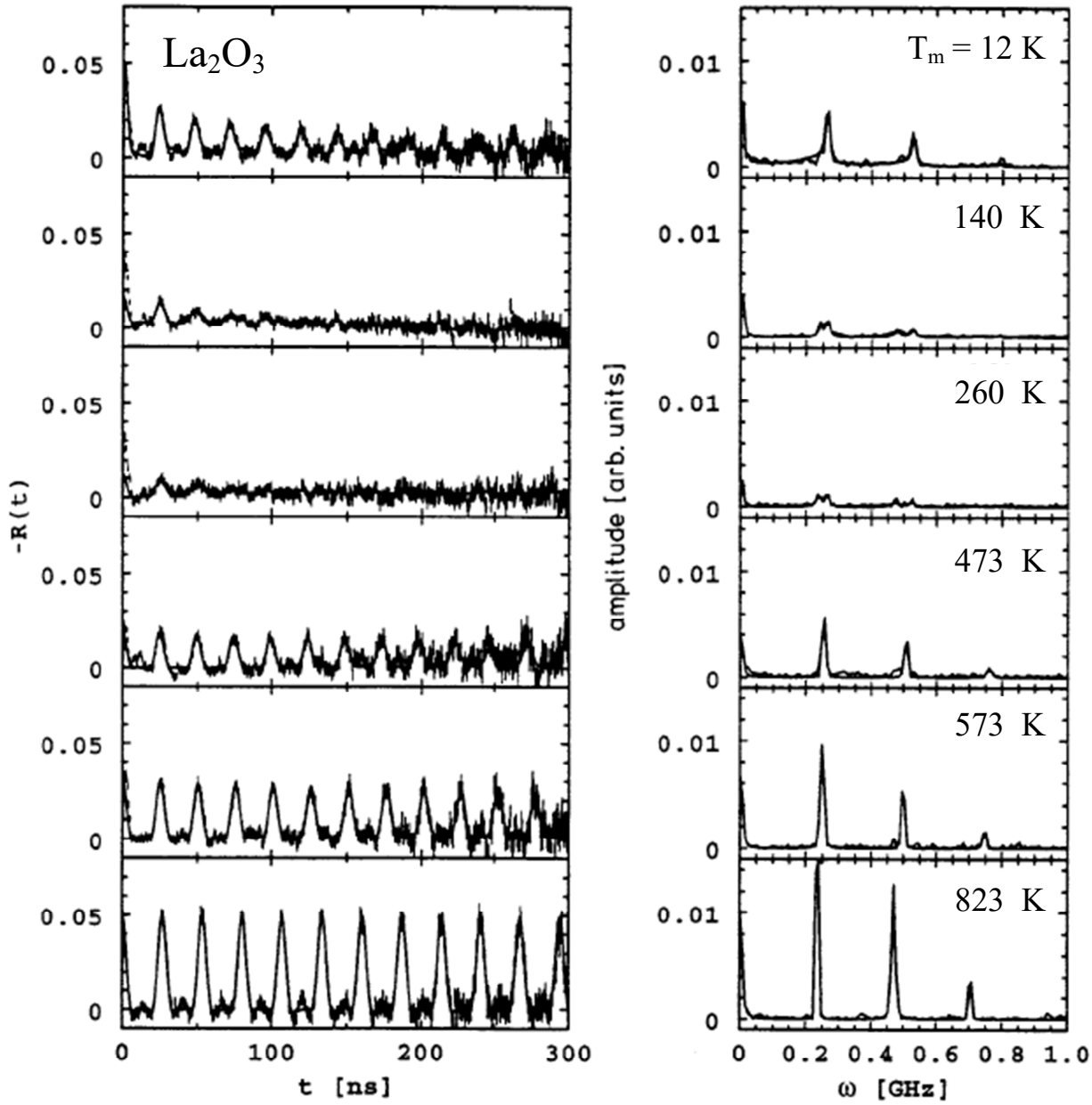

Fig. 2: R(t) spectra (left) and their Fourier transforms (right) of ^{111}In in La_2O_3 for different measuring temperatures. Reprinted figure with permission from D. Lupascu *et al.*, Phys. Rev. B 54, 871 (1996) [13]. Copyright 1996 by the American Physical Society.

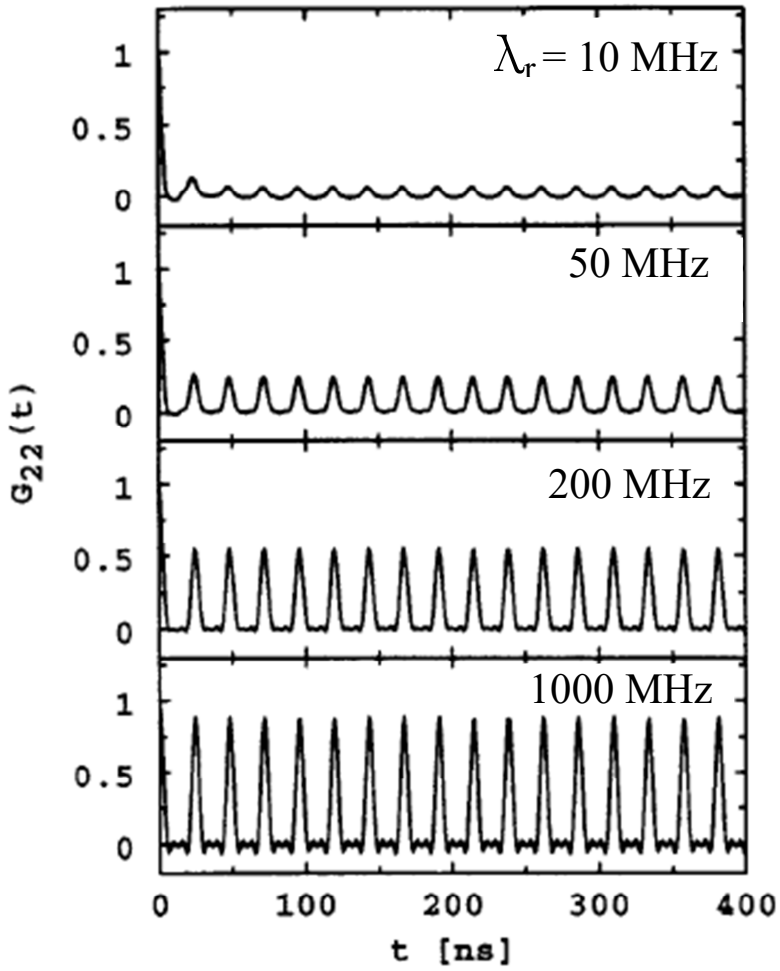

Fig. 3: Simulated spectra for ^{111}In in La_2O_3 for different recovery rates λ_r after emission of the first γ -ray. The displayed spectra were calculated for a transition rate between the initial EFG's of λ_i = 20 MHz. Reprinted figure with permission from D. Lupascu *et al.*, Phys. Rev. B 54, 871 (1996) [13]. Copyright 1996 by the American Physical Society.

When the atoms reach their electronic ground state (at the time t′) the hyperfine interaction will be static. Thus $G_{22}(t)$ may now be seen as an average of the perturbation factors affecting to the N probes. The perturbation factor, at time t, corresponding to a probe that arrives at the electronic ground state at time t′, is:

$$G_{22}(t,t') = \begin{cases} G_{22}^{s}(t)\exp(-\lambda_r t') & if \quad t' < t \\ G_{22}^{s}(t)\exp(-\lambda_r t) & if \quad t < t' \end{cases}$$

The average, taken on the N atoms, including those atoms that reach their ground state at time t′ before t and those that are still excited at time t is:

$$G_{22}(t) = N^{-1}\int_0^{\infty} G_{22}(t,t')P_g(t')dt'$$

$$G_{22}(t) = \left[\frac{\lambda_r}{\lambda_r+\lambda_g}\exp\left(-\left(\lambda_r+\lambda_g\right)t\right)+\frac{\lambda_g}{\lambda_r+\lambda_g}\right]G_{22}^{s}(t) \quad . \qquad [2]$$

This model cannot be distinguished from the physically different case where there are two fractions of probes, f_d undergoing a fluctuating field characterized by the perturbation factor

$$G_{22}(t) = G_{22}^{s}(t)\exp\left(-\lambda t\right) \qquad [3]$$

and f_s subjected only to the static field. Indeed, Eq. [2] is equivalent to:

$$G_{22}(t) = \left[f_d\exp(-\lambda t) + f_s\right]G_{22}^{s}(t) \ . \qquad [4]$$

Eq. [2] and [4] coincide if:

$$f_d = \lambda_r/\lambda \quad f_s = \lambda_g/\lambda \quad \lambda = \lambda_r + \lambda_g \ .$$

All these models have been used in the past for dealing with AE. Pasquevich *et al.* [14] have used Eq. [4] to analyze PAC results of Ga_2O_3:^{111}In. Very recently Sato *et al.* [73] have used the Bäverstam *et al.* model to discuss the local fields in the vicinity of ^{111}Cd probes in different ZnO samples (0.5 at.% inactive In-doped and undoped) by means of the PAC technique.* Penner and Vianden [12] have used Lupascu's approximation for analyzing their PAC results in Al_2O_3:^{111}In. Summarizing, a close description of the AE and their temperature dependence is still missing.

Examples of PAC studies performed on binary oxides using ^{111}Cd and ^{181}Ta impurity probes

A compilation of the PAC studies performed on binary oxides using ^{111}In(EC)^{111}Cd and ^{181}Hf(β^-)^{181}Ta impurities as probe-atoms is given in the appendix. If other way of production of the probes are used, this will be explicitly indicated. Results of selected experiments that have given by themselves important information are described for two specials cases below.

Indium Oxide. Indium oxide (In_2O_3) is a very important material for microelectronic applications [74]. It is widely used as a material for transparent electrodes in electronic devices such as liquid crystal displays [75], solar cells [76], as a barrier layer in tunnel junctions [77], as a sensing material in gas sensors [78] and in nanowire technology [79]. In_2O_3 occurs in the bixbyite structure, body-centered cubic (bcc, $Ia\bar{3}$, a=10.117 Å). All deposited In_2O_3 films show this cubic crystal structure. A rhombohedral (rh, $R\bar{3}C$, a=5.478 Å and c=14.51 Å) structure has been reported [80], but only few reports concerning the synthesis of Rh-In_2O_3 can be found in the literature [81,82].

*During the proofs reading of this chapter, E.L. Muñoz *et al.* reported a combined experimental and *ab initio* analysis of ECAE in Sc_2O_3:^{111}In using also the Bäverstam *et al.* model to fit the PAC spectra (Muñoz *et al*., Hyperfine Interact. , DOI: 10.1007/s10751-010-0207-2).

A variety of electrical properties of In_2O_3 thin films can be obtained (metallic, semiconducting, or insulating behavior). Highly conductive Sn doped In_2O_3 films are widely used as transparent electrodes in optoelectronic devices. Highly resistive In_2O_3 thin films are widely used as active layers of gas sensors [78], especially in ozone sensors.

Stoichiometric In_2O_3 is a transparent insulator that can be doped by substituting Sn for In to yield n-type indium tin oxide (ITO), a well-known transparent conductor. In contrast, Al_2O_3, which is isoelectronic with indium oxide and is another transparent insulator, cannot be effectively doped. A major difference between these two materials is that In is a multivalent cation as evidenced by the existence of several indium oxides: In_2O_3, InO and In_2O. In a simple integer-valence ionic model, the In valence decreases from 3+ to 2+ to 1+ in this sequence. Hence, the multivalent nature of In likely enables the In_2O_3 host electronic structure to accommodate the enormous conduction electron concentrations (of order $10^{20}/cm^3$ or more) typical of useful transparent conductors, and associated with the three indium oxides mentioned above [83].

Indium in In_2O_3 has electronic configuration In^{3+}: $[Kr]4d^{10}5s^05p^0$, hence the ion can add electrons to the empty 5*s* and 5*p* levels. Of course, substantial metal/oxygen hybridization occurs but, in general, adding electrons to energetically clustered bands will probably introduce optical transitions in the visible portion of the spectrum. Hence, for n-type transparent conductors, the conduction band minimum should be well separated energetically from higher lying bands. This condition is met in the elements Cd, In, Sn, Zn and Ga, all of which still have filled d-bands after reaction with oxygen [83].

In the context on hyperfine interactions studies of binary oxides using PAC and $^{111}In(EC)^{111}Cd$ as probe, In_2O_3 becomes very special because the starting probe is not an impurity in the compound. The hyperfine interactions can be studied without taking into account the binding of structural or electronic defects to the probe site, at least before de EC decay of ^{111}In to ^{111}Cd. While the local structure of the In site is well-known and the structural relaxations produced by the ^{111}Cd atom has been understood completely [30,32], open questions remain concerning the electronic configuration of the impurity center after the EC decay.

In 1956, Lehmann and Miller carried out the first PAC investigation on In_2O_3 doped with $^{111}In(EC)^{111}Cd$ [84]. Measuring at room temperature the angular correlations of the ^{111}Cd γ radiation, they found a PAC spectrum dramatically attenuated. This attenuation was attributed to the influence of the K-electron-capture. Latter on, in 1963, at the Uppsala meeting on "Extranuclear Perturbation on Angular Correlations", Frauenfelder coordinated a discussion about "*after-effects*" [85]. He introduced the topic as follows: " In ^{111}Cd one has a K-capture. After this capture, the radioactive atom can be described with a Swiss cheese model. First there is a hole in the innermost shell. Then, with a certain probability, about half or so, an X-ray will be emitted so that the hole moves out. The hole diffuses into the shells. In the following steps, as the energies of the electronic transitions decrease, the probability of Auger effects predominate on the probability of X-ray emissions. This results in the multiplication of the holes. As a final result the probe can get charges up to 20|e| or even more. It is known that the probe can get the ground state in a time of 10^{-13} s, when it is embedded in a metallic surrounding. The first γ -ray in the cascade of ^{111}Cd is emitted from a nuclear level, which decays with a mean lifetime of 120 ps, which is very much longer than the recovery time mentioned above. The questions were: what happens in an insulator where the electrons may be not available? Are there really *after-effects*? "

In 1964, Salomon [86] found that the attenuation of the PAC spectrum of $^{111}In(EC)^{111}Cd$ in In_2O_3 can be removed by increasing the measuring temperature. Twenty years later, Bibiloni *et al.* [10] showed that the recovering of the PAC spectra with temperature can be related to the increase of the electron availability at the probe site. In turn, this increase is related to the semi conductive nature of In_2O_3. At the same time, the two EFGs that are the signature for probes located at the two non-equivalent cation sites (called D and C) of the cubic bixbyite structure of this oxide where identified by different PAC groups [10,87].

In In_2O_3 the cations reside at the centre of two oxygen octahedra with quite different geometry and cation-oxygen bond-length. Furthermore, the crystallographic abundance is well reproduced by the

observed fractions of the two mentioned EFGs [10, 87,88]. The method of introducing the ^{111}In probes (during the chemical synthesis, by implantation or diffusion) does not change the general result: evidently the radioactive probes find the correct crystallographic sites in their ‘‘own’’ oxide. Among the binary oxides, there are many sesquioxides that crystallize in the same bixbyite structure having lattice constants in a wide range from 0.94 to 1.09 nm. This group takes its name from the mineral $(Fe,Mn)_2O_3$, called bixbyite. The cations form a nearly cubic face center lattice in which six out of the eight tetrahedral sites are occupied by oxygen atoms. The elementary cell of the oxide lattice consists of eight such cubes, containing 32 cations and 48 O^{2-} ions. The structure is characterized by two nonequivalent sites for the cations, called “C” and “D” for their point group symmetry, both coordinated with six oxygen atoms. Their abundance in the lattice is 3:1. Site D is axially symmetric and can be described as surrounded by six oxygen atoms at the corners of a distorted cube, leaving free two corners of a body diagonal. In site C the cube is more distorted and the six oxygen atoms leave free the two corners on a face diagonal. The distribution of the nearest oxygen neighbors around the cations in each site are represented in Figure 4. The real situation has been approximated by a cube that keeps the main symmetry properties of the sites. The simplest model used to predict the EFG in a solid is the point charge model (PCM). In this model the atoms are replaced by punctual charges usually selected according to the nominal valence (z_k) of the ions in the lattice. Locating the origin of coordinates at the site of interest, the lattice contribution to the EFG tensor V_{ij}^{latt} at this site can be calculated as the direct sum of the contributions from each charge ez_k:

$$V_{ij}^{latt} = \frac{e}{4\pi\varepsilon_o}\sum_k z_k \frac{\left(3x_{ki}x_{kj} - \delta_{ij}r_k^2\right)}{r_k^5},$$

where the sum extends to all the ions in the lattice. In this model the contribution of the deformed core electron shells of the probe-atom, located at the site of interest, due to their interaction with the rest of the ions is taken into account through the Sternheimer antishielding factor γ_∞, amplifying the lattice contribution:

$$V_{ij}^{\exp} = (1-\gamma_\infty)V_{ij}^{latt}.$$

In this context, the EFG produced at each cation site in a bixbyite by the nearest neighbor ions can be calculated assuming that the oxygen ions have equal charge. This calculation gives the following values and ratios of the EFG components at each site:

$V_{zz}(C)/V_{zz}(D) = -0.5$, $\eta_C = 1.$ and $\eta_D = 0.$

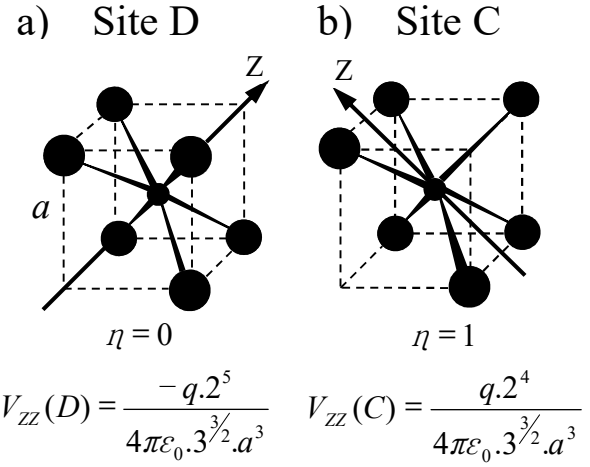

Fig. 4: Oversimplified scheme of the oxygen distribution around each cationic site in the bixbyite structure: (a) site D, (b) site C. The arrows denote the EFG principal axes in each case. In the case of Site C, the axes Y and Z can be interchanged since $\eta = 1$ does not allow distinguishing between them. In the real structures the oxygen atoms are slightly displaced from the corners of the cube.

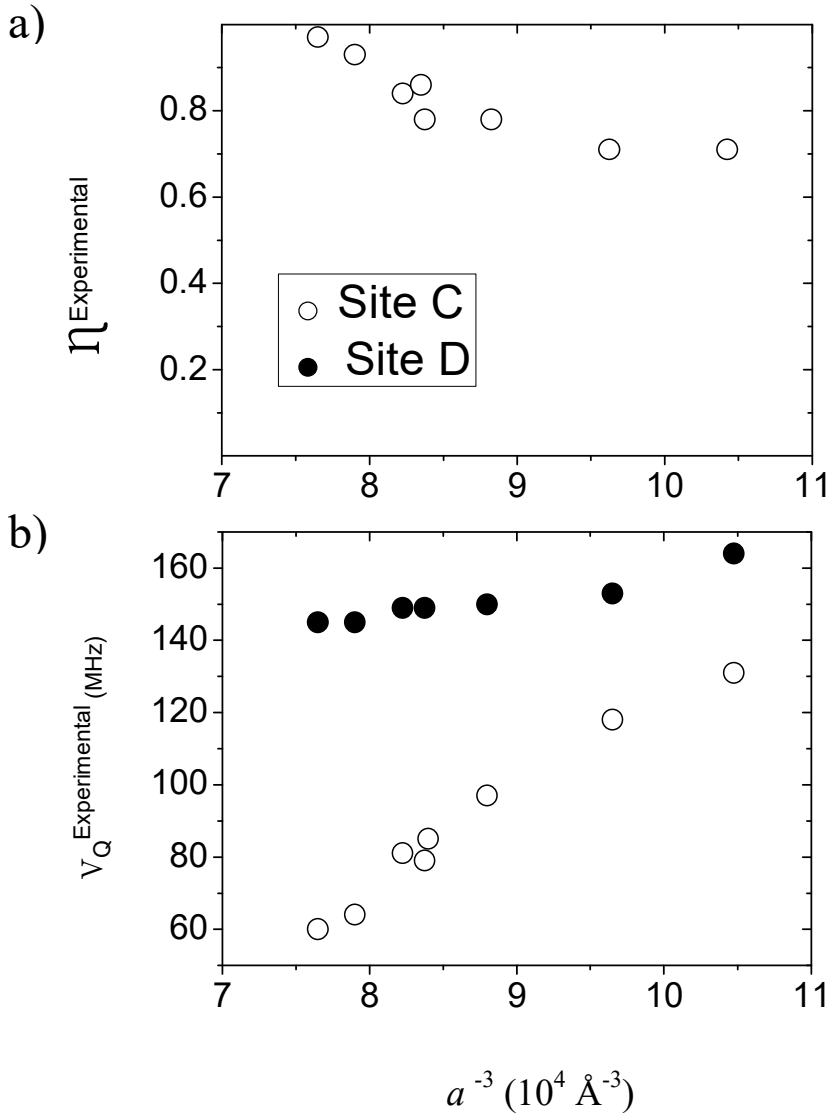

Fig. 5: (a) The dependence of the hyperfine parameters ν_Q for ^{111}In(EC)^{111}Cd probes on both sites D and C of the bixbyite structure on a^{-3}, where a is the lattice constant. (b) The asymmetry parameter η(C) varies slowly with a^{-3}, whereas η(D) = 0 remains for all bixbyites. Recreated from Ref. [89].

As these oxides show nearly pure ionic binding character the strength of the EFG at the cationic lattice site could be expected to be proportional to d^{-3}, where d represents a typical distance to neighboring oxygen ions. Therefore, the group of bixbyite oxides gave a unique chance to study the influence of the lattice size on the observed EFG. As shown in Fig. 5 the measured quadrupole frequencies ν_Q on both sites scale nearly linearly with a^{-3} (a is the lattice constant) in the whole bixbyite crystal-class [89]. In more detail, the following information on the local structure can be obtained: For site D, the deviation from the linearity of ν_Q(D) with a^{-3} is small and axial symmetry ($\eta_D \approx 0$) is observed for all oxides. For site C a dramatic increase of ν_Q(C) and a non-linear decrease of η_C with a^{-3} is found. The straightforward interpretation is that the octahedron around site D, even if they relax, remains with axial symmetry through the bixbyite series, while the

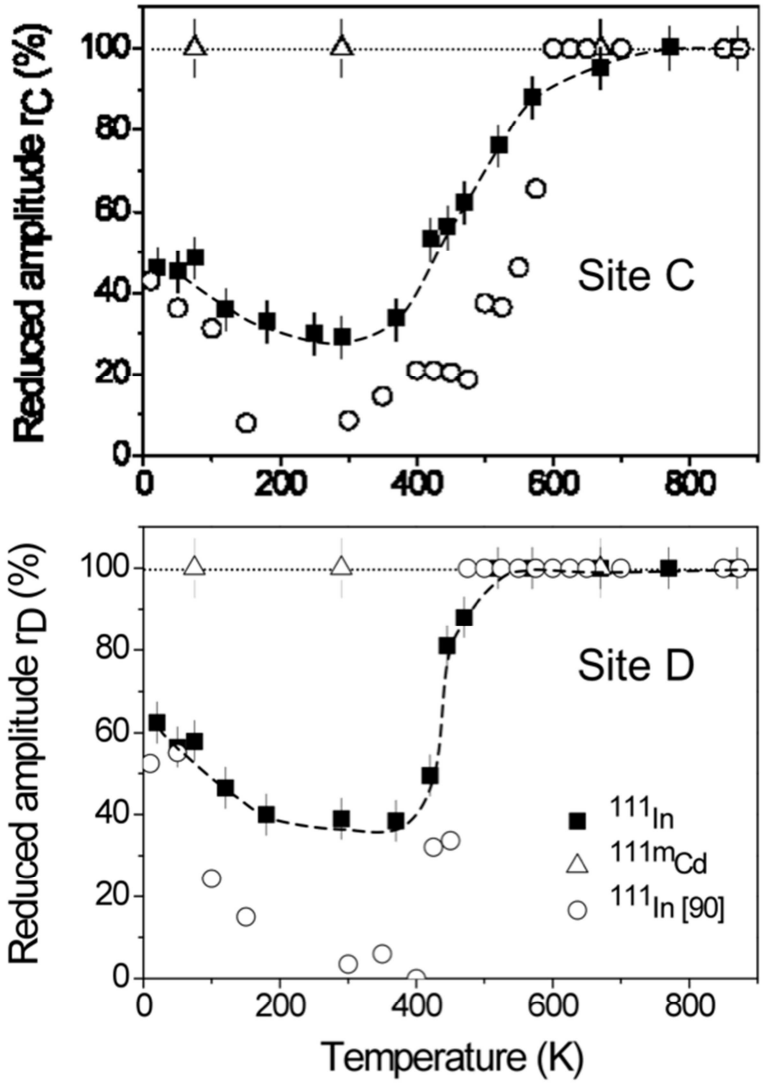

Fig. 6: Reduced amplitude of the perturbation function of ^{111}In(EC)^{111}Cd- probes implanted in In_2O_3 plotted versus the measuring temperature for both sites C and D. Included are data obtained at ISOLDE after implantation of ^{111m}Cd into In_2O_3. Recent data obtained at IPEN using ^{111}In-diffused in In_2O_3 powder samples are shown for comparison [90]. Recreated from Refs. [1,11].

irregular octahedron around site C are increasingly deformed with increasing lattice constant, as shown by the η_C behavior.

As already mentioned, the first paper on the application of the PAC technique to an oxide found the electron-capture AE for ^{111}In(EC)^{111}Cd probes in In_2O_3 [84]. The ^{111}In isotope decays via EC to the 7/2+ state of ^{111}Cd and, with a mean life time of 170 ps, the first γ quanta of the PAC cascade is emitted. The EC-decay caused a hole in the K-shell, which is filled and followed by X-ray and/or Auger transitions. Within 0.01 ps further Auger processes produce additional holes in higher shells. Therefore, the ^{111}Cd-atom is highly ionized after its creation and electrons are needed to stabilize its electron shells. It depends strongly on the properties of the matrix (metal, semiconductor, and insulator) whether enough electrons are available in time or not. In metals the missing electrons are fast supplied quickly and no AE are observed. But in semiconductors or insulators the relaxation time of the excited electron shell may be longer than the mean lifetime of the hyperfine-sensitive intermediate state in ^{111}Cd ($\tau \approx 121$ ns), leading to time-dependent (fluctuating) EFGs (giving rise to a *dynamic hyperfine interaction*) and hence to damped $G_{22}(t)$ PAC perturbation functions. Many different experiments have proven that the EC AE is, without doubts, the origin of this damping of the R(t) functions. Implantations at ISOLDE/CERN of the $T_{1/2}$ = 48 min isotope ^{111m}Cd

into different bixbyite oxides showed no AE [1,11] (see Fig.6). The number of ^{111}In probes that senses a dynamic interaction at a certain temperature in In_2O_3 seems to depend also on the nature of the sample, as shown in Fig. 6 by the results of recent experiments performed at IPEN/São Paulo * [90].

Furthermore, the absence of attenuations at room temperature was observed in the PAC experiments with the ^{181}Hf(β^-)^{181}Ta probe in this oxide [91] (see Fig. 7). This observation is also valid for the rest of the bixbyites studied with the ^{181}Hf probe [29, 35,92-96].

In the two examples given above (experiments using ^{111m}Cd and ^{181}Hf), no EC-decay can distort the probe's electron shell creating additional electronic holes. It is very interesting to mention here that the EFG measured with ^{111}Cd and ^{111m}Cd are equal, reflecting the same electron density in the neighborhood of the probe-atom. This fact is in excellent agreement with the results obtained in the *ab initio* calculations in Cd-doped In_2O_3 performed almost 20 years later than the first experiments. In effect, the experimental EFG is exactly reproduced if the ionized (Cd^-) state of the impurity (one trapped electron) is considered [31]. If one hole is present, the predicted EFG at site C change aprox. 50% [97].

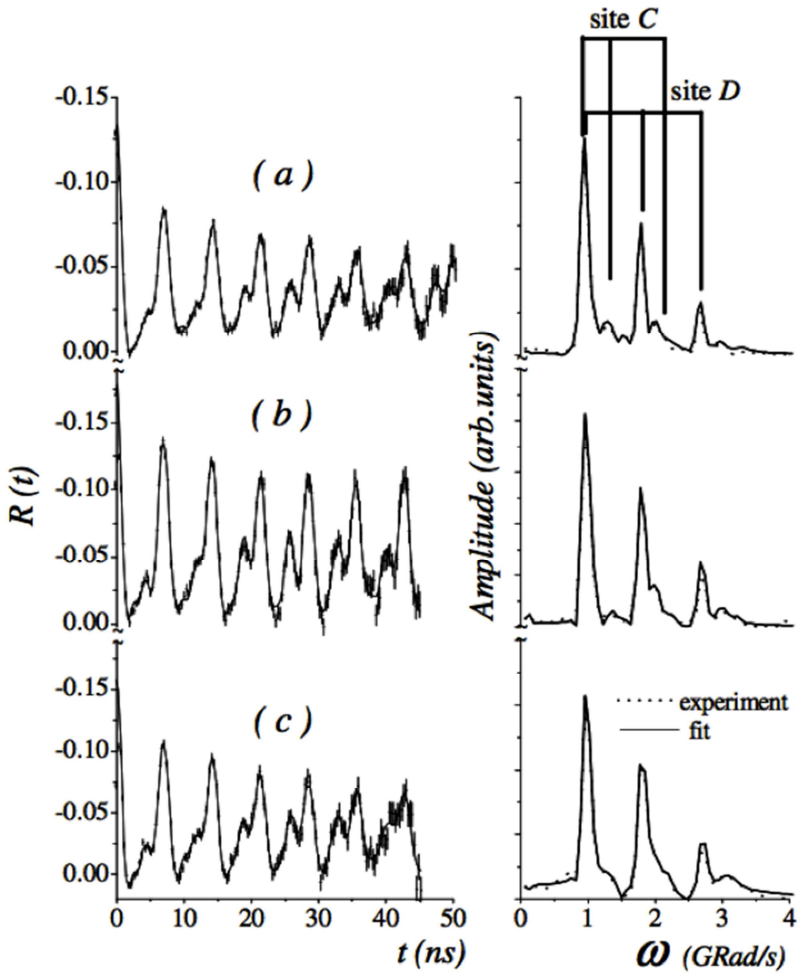

Fig. 7: PAC spectra (left) and their Fourier spectra (right) measured at RT on: (a) chemically prepared In_2O_3:^{181}Hf annealed 1 h at 1303 K, (b) ^{181}Hf-implanted in ''crystalline'' In_2O_3 thin film annealed 1 h at 1273 K and (c) ^{181}Hf-implanted amorphous In_2O_3 thin film annealed 1 h at 1273 K. Reprinted figure with permission from M. Rentería *et al.*, Phys. Rev. B 55, 14200 (1997) [91]. Copyright 1997 by the American Physical Society.

*Instituto de Pesquisas Energéticas y Nucleares (IPEN), São Paulo, Brazil

An alternative approach to test the presence of the AE is to dope the oxides with different amounts of donors to increase the availability of electrons at the ^{111}In(EC)^{111}Cd probes. In In_2O_3 this was done with tin [88]. The existence of these AE depends on the oxide purity. An interesting example of this dependence is given by Quille *et al.* [98]. In that work, a equimolar mixture of CdO and In_2O_3 was doped with ^{111}In and overnight calcinated at 1273 K in normal air atmosphere, the result was In_2O_3 doped with Cd (CdO discomposes below 1273 K and Cd has a boiling point of 1138 K). PAC results obtained at room temperature (RT) and at 613 K are shown in Fig. 8b. In a second process, In_2O_3 doped with C was made, following a procedure described by Weiher [99], which consists in heating, at 1273 K, a mixture of indium metal and carbon, in a loosely covered porcelain crucible. In this way crystals of In_2O_3 grew on the walls and cover of the crucible. Later the crystals were doped by with ^{111}In. PAC results obtained at RT and at 613 K are shown in Fig 8a.
The presence of AE, at room temperature, is clearly evident in the case of doping with the acceptor impurity Cd while, in the case of doping with C, a donor, there is no change of the spectra with

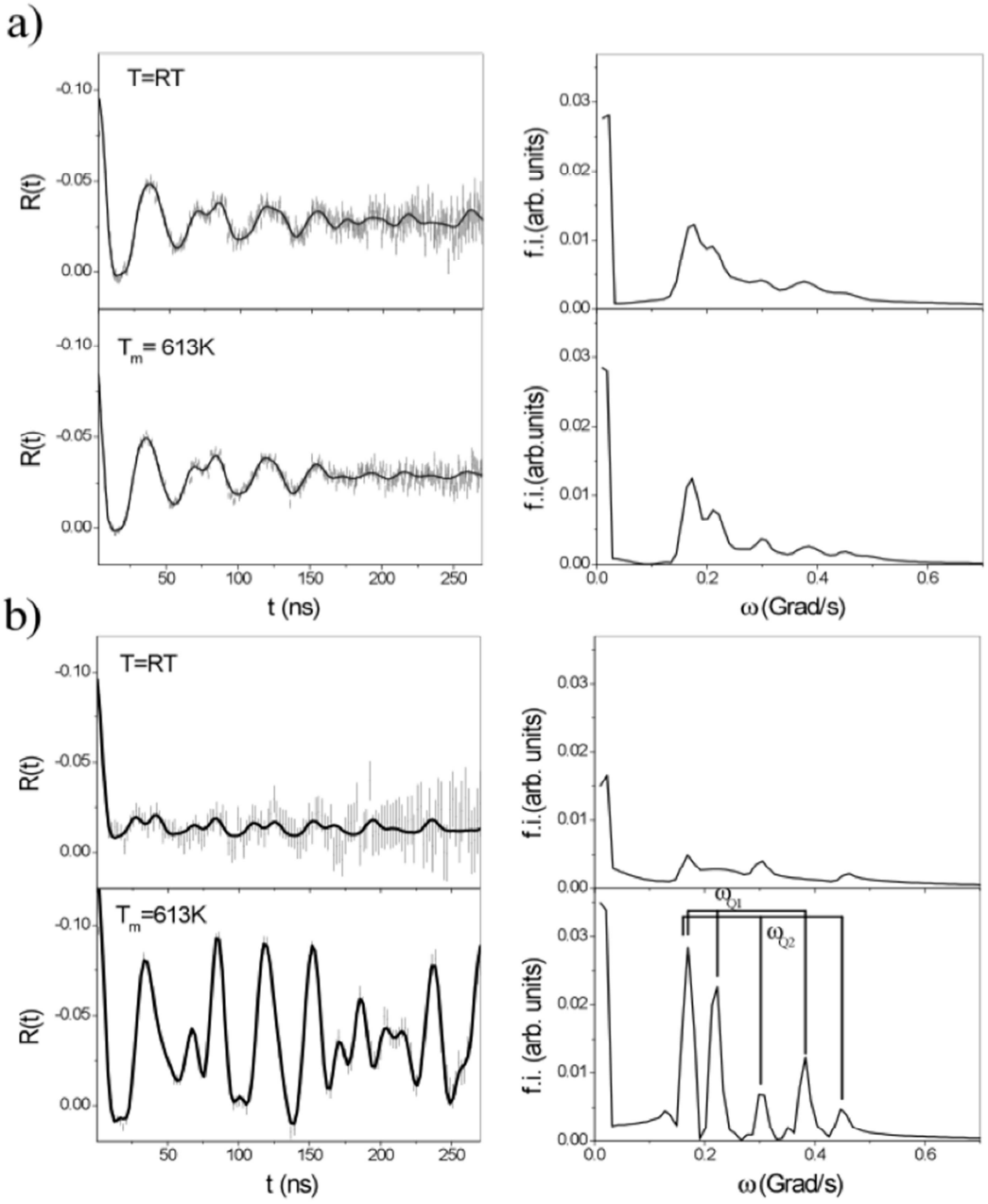

Fig. 8: PAC spectra and their Fourier transforms, obtained at room temperature and at T = 613 K , corresponding to (a) In_2O_3 doped with C and (b) In_2O_3 doped with Cd . Data taken from Ref. [98].

temperature. The different attenuation observed in the spectra measured at 613 K corresponds to different impurity content of the samples.

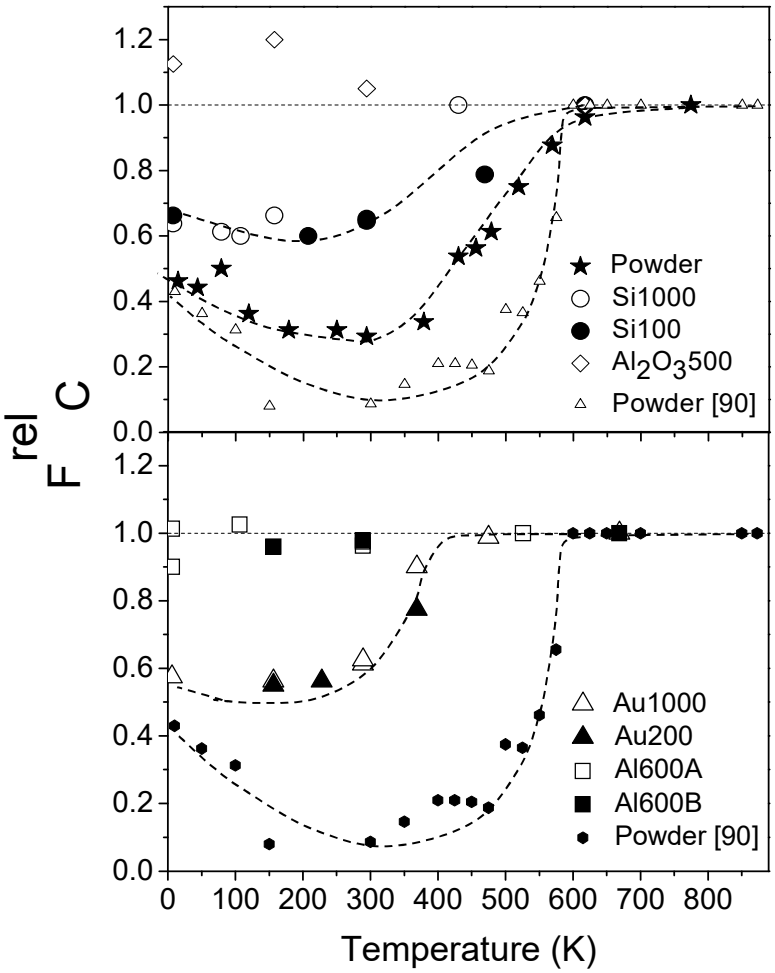

Fig. 9: Reduced amplitude of the perturbation function of ^{111}In probes located at site C in In_2O_3 films with different thickness on different types of substrates. The name of the data points contains the substrate and the film thickness in nanometers. Recent data obtained at IPEN using ^{111}In-diffused in In_2O_3 powder samples are shown for comparison [90]. Recreated from Refs. [1,11].

In 1987, Bolse *et al*. [100] published a ^{111}In(EC)^{111}Cd PAC study on a thin In_2O_3 film on an Al substrate, in which no dynamic interaction was present, in contrast to the results obtained in bulk samples. Later, Lohstroh *et al*. [11] investigated this system in detail to find out, whether electrons can be ‘‘injected’’ from the substrate into the film or not. ^{111}In ions were implanted into In_2O_3 films of various thickness (100–1000 nm), which were deposited onto different substrates (Au, Al, Si, Al_2O_3) to vary the availability of the electrons. Detailed analysis showed later the unintended presence of small amounts of dopants [1]. Figure 9 gives an overview of the results, again as a plot of the temperature dependence of the reduced amplitude.

The idea that the electronic structure of the probe might contribute strongly to the EFG in binary oxides, triggered a new variation of the experiments. The second commonly used PAC probe is ^{181}Hf, which decays via β^- to ^{181}Ta. This second probe, introduced in the same systems studied with ^{111}Cd, allows to study the influence of the electronic configuration of the impurity probe atom itself on the EFG. From the early nineties, many crystal structures have been implanted with ^{181}Hf probes [29,35,37,91-96,101,102], especially the class of bixbyite oxides. Among this group, twelve oxides with the same crystalline structure have been compared and the data show that in all these oxides,

after implantation and subsequent high temperature annealing the ^{181}Hf probes occupy two sites that have been identified as the two non-equivalent cation sites of the bixbyite structure, the same as with the ^{111}In(EC)^{111}Cd probe.

The results obtained for In_2O_3 show that the ratio $\nu_Q(C)/\nu_Q(D)$ for both ^{111}Cd and ^{181}Ta probe nuclei are coincident, as Fig. 10a displays. This is true in the range of the lattice parameter *a* corresponding from In to Dy sesquioxides. The values systematically depart from the value of 0.5 obtained using the PCM with the approximation of "undistorted cubes" described above. At present, this is not surprising since the structural relaxations introduced by the ^{111}Cd impurity in the real case can modify the symmetry of the cation coordination at site C as *a* decreases, as we have learned from the *ab initio* calculations, increasing the EFG.

In the past, it was asked in numerous discussions whether the inserted PAC probes are really "good observers" – only observing – or if they actually change their neighborhood, that they are supposed to analyze. The approximate coincidence of the ratio shown in Fig. 10a for both ^{111}Cd and ^{181}Ta probes, which tries to cancel the contribution of the probes to the EFG letting the dependence on the structure of the cation site (if a multiplicative model for the EFG applies), induced to think at a first glance that both probes must be seeing the same structure. Unfortunately we can not use the PCM to go deeper in the analysis of these ratios since the PCM fails in the description of the experimental EFGs, as Fig. 11 clearly shows. Moreover, when all the bixbyites reported in Table II are plotted in this systematics it can be seen in Fig. 10b and 11 that the relative trends for sites C and D are not the same for both probes. Perhaps that coincidence, or better that shown in Fig. 12 for any site in any bixbyite, may be showing the fact that the probe tries to reconstruct its neighborhood like in its own oxide, as will be explained below.

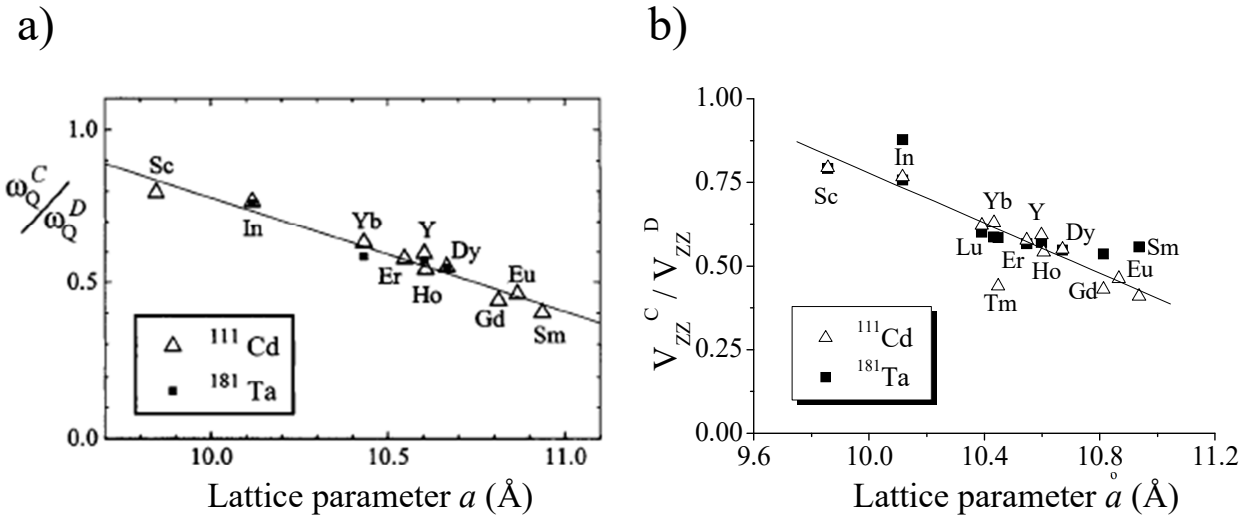

Fig. 10: (a) Ratio of the nuclear quadrupole frequencies ω_Q of site C to that of site D in bixbyites. Reprinted figure with permission from M. Rentería *et al.*, Phys. Rev. B 55, 14200 (1997) [91]. Copyright 1997 by the American Physical Society. (b) Ratio of the EFG of site C to that of site D in bixbyites using the data given in Tables I and II. The upper data point for In_2O_3(^{181}Ta) in Fig 10b comes from a new determination and QI assignment enlighten by recent *ab initio* calculations [35].

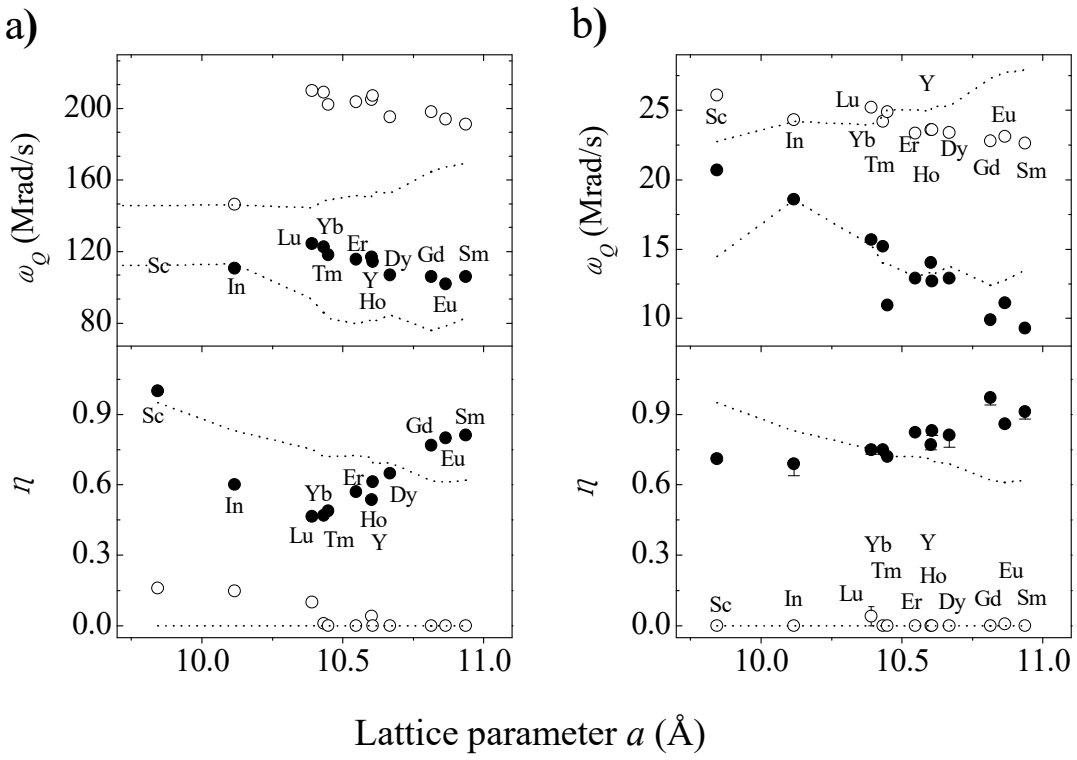

Fig. 11: a) Experimental nuclear quadrupole frequency ω_Q and asymmetry parameter η measured at RT for substitutional (a) ^{181}Ta and (b) ^{111}Cd impurities at sites *C* (black) and *D* (hollow) in bixbyites plotted as a function of the lattice parameter *a*. The errors are smaller than the symbols. Dotted lines are the PCM predictions. The PCM predictions for ω_Q are normalized to the In_2O_3 values for both probes. Recreated from Ref. [29].

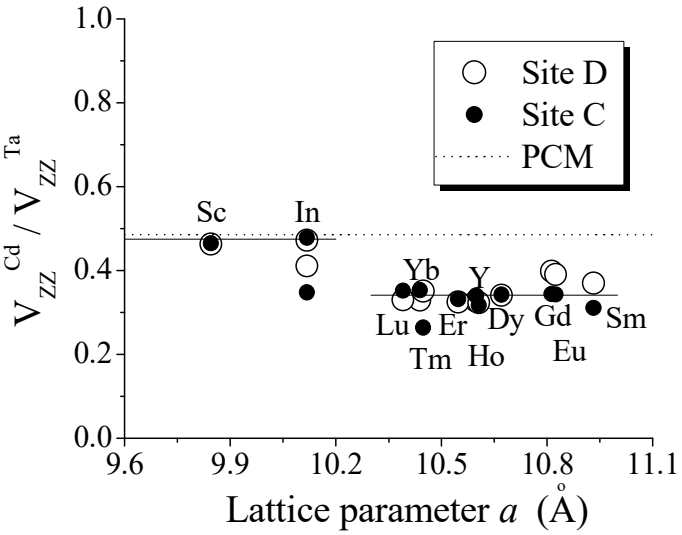

Fig. 12: V_{ZZ}^{Cd}/ V_{ZZ}^{Ta} for both sites C and D and all the bixbyites. The solid line is just to guide the eye. Recreated from Ref. [92]. The lower data points for In come from the new determination on In_2O_3:^{181}Ta [35].

The body of data from the bixbyites gave the answer that the probe senses different EFGs in the different oxides, controlled by the local structure of each cation site of each oxide of the series and by the electronic configuration of the probe-atom [29,91,95]. Now, from the *ab initio* calculations it turned out that distortions around the ^{111}Cd [18,27,31-34,37,103] and ^{181}Ta [34-37] probe-atoms occur, modifying their neighborhood.

Already with the simple PCM there had been cases where the position of some neighboring atoms to the probe had to be modified to achieve a better agreement between the experimental data and the calculation. For example, in the case of TiO_2 it was argued that the ^{111}Cd ion is larger than the Ti ions. A positive distortion of 0.04 Å of all six oxygen neighbors away from the probe reproduced the measured EFG [104]. One year before a similar idea had been proposed to match the experimental EFG tensor with the PCM prediction for the case of SnO_2:^{111}Cd [105]. However, these agreements obtained for the EFG were fortuitous since the *ab initio* calculations have shown that the relaxations are strongly anisotropic in Cd-doped TiO_2 and SnO_2. A much larger distortion was also proposed in Cr_2O_3:^{111}Cd [106]. The observed EFGs were explained in the PCM by shifting the position of the In atoms from the substitutional Cr sites 0.29 Å along the [0 0 0 1] axis towards the empty octahedral interstitial sites. In this case, *ab initio* calculations of Darriba *et al.* [37] predict such a displacement of the Cd atoms but also relaxations of the nearest oxygen ions.

When already the old PCM calculations gave hints to distortions of the lattice due to the probe atoms in certain binary oxides, today the accuracy of the *ab initio* DFT calculations using the APW+lo method clearly depend upon the precise knowledge of these distortions. In this kind of calculations, electronic and structural effects, introduced into the semiconducting oxide hosts by the presence of the impurity probe (impurity levels, structural atomic relaxations, charge state of the impurity, etc.), can be described self consistently without the use of arbitrary suppositions. An extensive discussion on the subject can be found in the literature [27,29,30]. In all calculated cases in binary oxides, the amount of distortion per atom decreases rapidly from the impurity nearest oxygen neighbors to the other shells. ^{111}Cd on both sites of In_2O_3 caused relaxations of about 5% of the nearest oxygen neighbors (ONN) of the Cd impurity [31,32]. In the case of ^{181}Ta it produces contractions of the ONN in the order of 7-8% [35]. From the excellent agreement between all the *ab initio* EFG calculations reported at present and the experimental PAC results it was concluded that the Cd and Ta impurities in binary oxides try to reconstruct their environment in their own oxides, CdO and TaO_2 [29,30,37]. Hence, the mentioned relaxations and contractions are explained by the smaller (larger) Ta-O (Cd-O) bondlenght in tantalum oxide (cadmium oxide)) with respect to the In-O distance in In_2O_3.

Hafnium oxide. Hafnia (HfO_2) is a wide band-gap semiconductor with a large dielectric constant. This oxide has a monoclinic structure at room temperature, transform to tetragonal structures at moderate temperatures, and to cubic structures at high temperatures. HfO_2 presents great technological importance because of its high melting point, high chemical stability, and large dielectric constant. In various forms and with the addition of small amounts of impurities, it has applications ranging from solid oxide fuel cell electrolytes to catalyst substrates and protective coatings [107-111].

HfO_2 is of particular interest because of its applications for electronic devices. HfO_2 is a high-k dielectric material ($\varepsilon \approx 25$) and a wide band gap oxide ($E_g \approx 5.7$ eV). Owing to its high thermal stability and low leakage current, it is replacing silicon dioxide as a gate material for silicon metal-oxide-semiconductor-field-effect transistors. In an ionic picture, the Hf^{4+} ion has a closed shell [Xe] $4f^{14}$ configuration and consequently it is nonmagnetic. Thus the observation of a ferromagnetic-like and strongly anisotropic behavior, well above room temperature, without magnetic 3*d* element substitution such as Co or Mn (elements more often used in semiconductors) is very intriguing [50,112]. Later on several experimental studies on the magnetic properties of HfO_2 thin films were reported in the literature with very controversial results [113]. Actually if the magnetic property is confirmed, it would widen substantially its application in the field of spintronics. Furthermore, HfO_2 is a simple material and a good model to study the origin of this unconventional ferromagnetism.

In the context of hyperfine interactions studies of binary oxides using PAC and ^{181}Hf (β^-) ^{181}Ta as probe, HfO_2 becomes very special because the starting probe is not an impurity in the compound. The hyperfine interactions can be studied without taking into account the binding of structural or electronic defects to the probe site, at least before the β^- decay to ^{181}Ta. This fact, the advantages of the γ - γ cascade of ^{181}Ta for PAC measurements, and the technological importance of hafnium oxide, has motivated several PAC investigations in the last years. In addition, ^{181}Hf ($T_{1/2}$ = 42d) is easily produced by thermal neutron capture: ^{180}Hf (n, γ)^{181}Hf.

The quadrupole interaction (QI) of ^{181}Ta in commercial coarse-grained HfO_2 has been extensively investigated in the past [114-120], and the results for the absolute values of the QI parameters and their temperature dependence obtained by different authors agree well between them. More recently, investigations of thin films [121, 122] and nanoparticles [123] of HfO_2 have been reported. The last reference is particularly important for this chapter. Indeed, the formation of probe-defect complexes (and insights into the nature of these defects) in hafnia nanoparticles was studied in great detail as a function of the thermal history of the samples by Forker *et al*. [123] by means of PAC experiments using ^{181}Ta as probe.

Before the results obtained by Forker *et al*. using hafnia nanoparticles are discussed, it is important to describe the results, obtained by the same group, in commercial coarse-grained (cg) HfO_2. Figure 13 shows typical PAC spectra of ^{181}Ta in cg-HfO_2 at different temperatures. Two components are required for a description of the room temperature spectra in the as purchased state. The dominant component with the well known QI parameters of m-HfO_2 [120] has a relative intensity of f_1 = 75%. The QI parameters of ^{181}Ta in the monoclinic phase at 300 K are the following:

I – monoclinic:	f_1= 75%	ν_Q = 793 MHz	η = 0.35	δ = 0.07
II – QI distribution :	f_2 = 25%	ν_Q =1300 MHz	η = 0.3-0.4	δ = 0.4

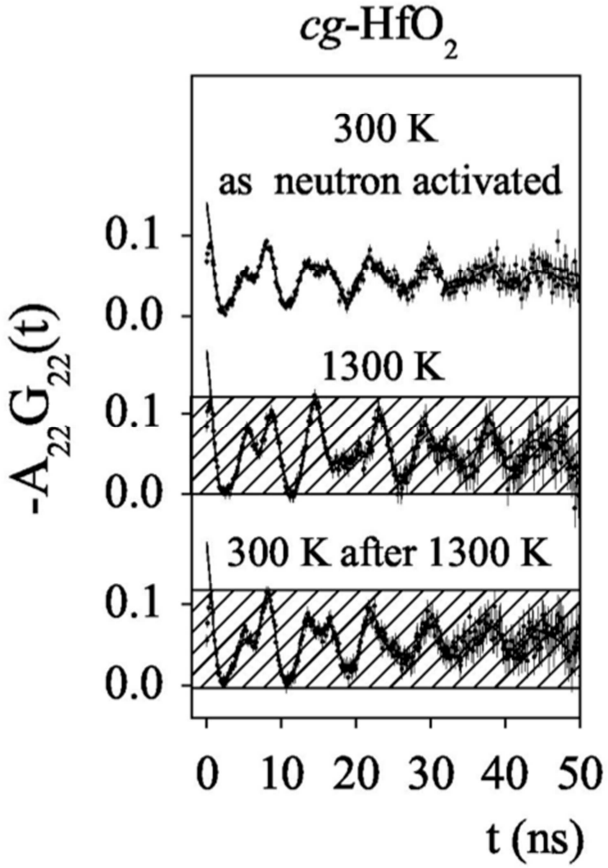

Fig. 13: PAC spectra of ^{181}Ta in powder samples (in vacuum) of coarse-grained HfO_2 at different temperatures. The height of the striped area is a measure of the monoclinic fraction at 1300K. Recreated figure with permission from M. Forker *et al.*, Phys. Rev. B 77, 54108 (2008) [123]. Copyright 2008 by the American Physical Society.

The temperature dependence agrees with that reported in a previous work [120]. The minority component II mainly shows up in the fact that the value of the anisotropy needed to describe the spectra at delay times t>5 ns is substantially smaller than the experimentally determined A_{22}. This implies that the perturbation factor of this fraction decreases rapidly within the first few nanoseconds. At larger delay times, the PAC pattern contains no other oscillatory components than those of the monoclinic oxide. The interaction of component II is, therefore, difficult to identify. Forker *et al*. discussed two possibilities: The fast initial decrease might reflect either a static distribution of strong QIs or be caused by a fluctuating interaction. The data given above correspond to the first possibility. In the case of a slow fluctuation of the QI, the perturbation factor can be approximated [61,124] by Eq.1.

Although Forker e*t al.* made an extensive and intensive study of n-HfO_2, using non-coated and alumina coated nanoparticles, produced using different precursors, and complementing the experiments with studies of n-ZrO_2, we will restrict the present description to the case of bare n-HfO_2 (as powder or pellets). In all cases, two samples of the oxide were studied, one subjected to continuous heating and cooling and the other cycled between temperature T and 300 K, respectively.

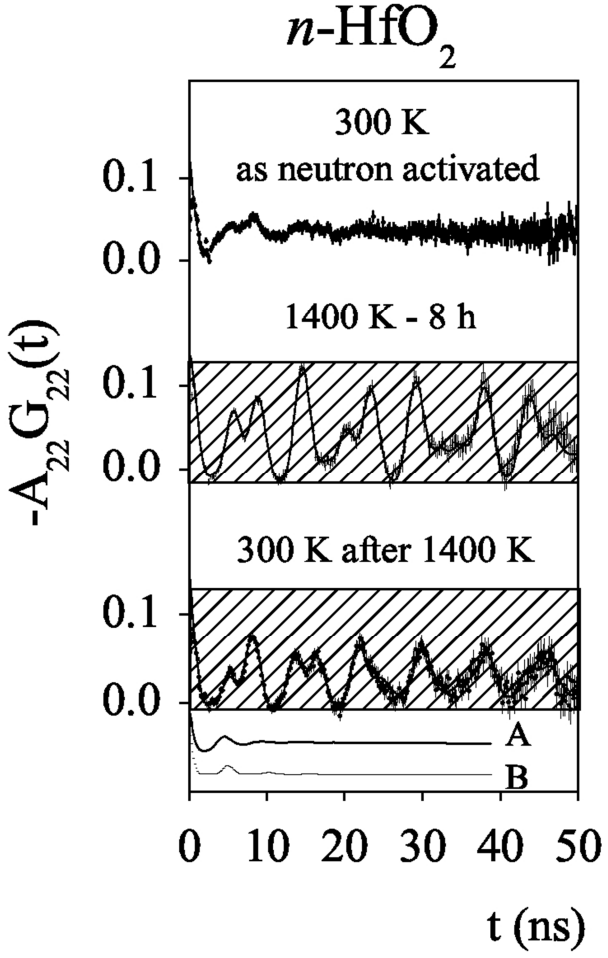

Fig. 14: PAC spectra of ^{181}Ta in powder samples (in vacuum) of HfO_2 nanoparticles at different temperatures. The height of the hatched area is a measure of the monoclinic fraction of n-HfO_2 at 1400K. Curves A and B give account of the two possibilities for the "defect component":
A: a static distribution of strong QIs.
B: a fluctuating interaction.
Recreated figure with permission from M. Forker *et al.*, Phys. Rev. B 77, 54108 (2008) [123]. Copyright 2008 by the American Physical Society.

Figure 14 shows how the PAC pattern of cg-HfO_2 oxide is reached at T~ 1400 K. Figures 15 and 16 show the relative intensity *f* and the relative linewidth δ of the monoclinic phase of the n-HfO_2 as a function of temperature. Figure 15 illustrates the typical behavior found in a continuous heating and cooling program; figure 16 the behavior found in a cycling experiment. In all the cases, the monoclinic fraction at T increases with temperature to reach saturation *f*~0.95 at T<1200 K. The increase of the monoclinic fraction *f* is accompanied by an irreversible decrease of the QI linewidth δ. Forker *et al*. shows that the degree of order characterized by the linewidth δ and the grain size *d* are correlated: The sharper the X-ray diffraction (XRD) lines, the less the damping of the oscillation amplitudes of the PAC spectra. The correlation $\delta \propto 1/d$ has also been observed in the ^{181}Ta PAC spectra of nanocrystalline TiO_2 [125].

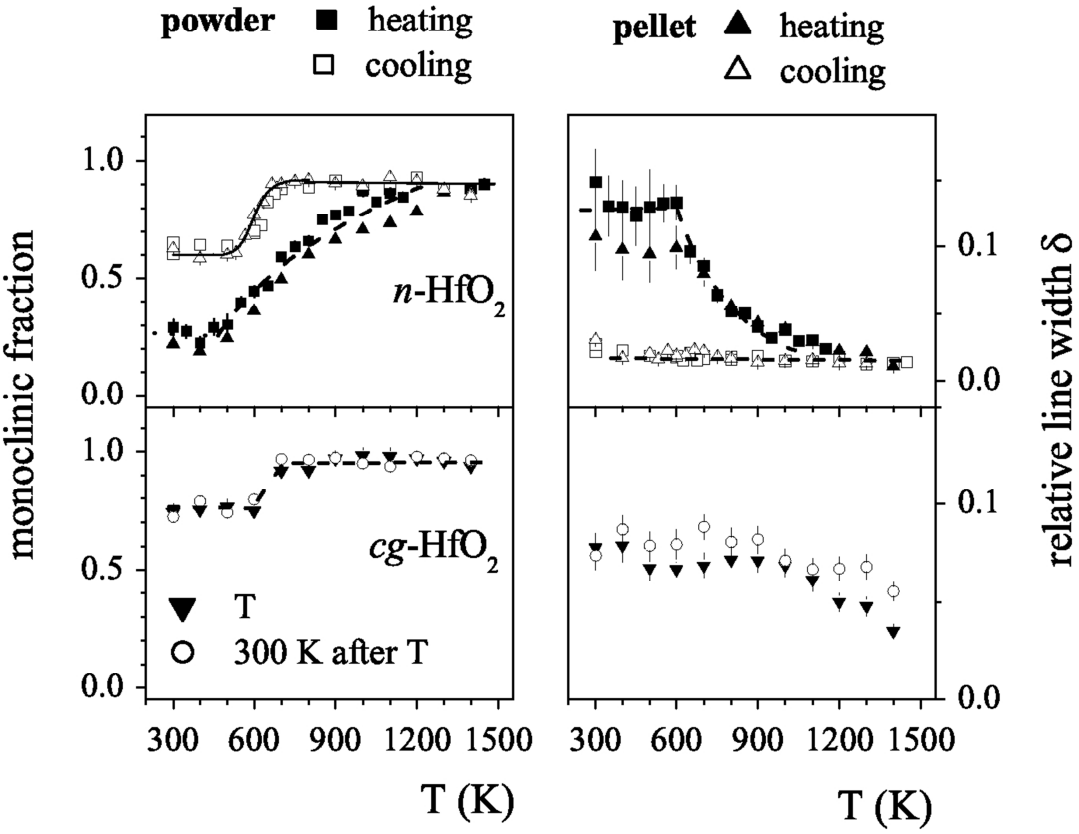

Fig. 15: The monoclinic fraction and the relative line width of the QI of ^{181}Ta in nanoparticles of HfO_2 and coarse-grained HfO_2 as a function of temperature. Data for nano-oxide powders and pellets are shown. The nanoparticles were continuously heated to T < 1550 K and cooled back to 300 K, whereas the coarse-grained oxide was cycled between temperature T and 300 K. For cg-HfO_2, the plot shows at a given T both the monoclinic fraction *f* (T) measured at this temperature (solid downward triangles) and the fraction *f*(300 K) (open circles) observed at 300 K after cooling from T. Note that *f* (300 K) = *f* (T) for all T. The solid lines at T<800 K represent fits (using the *two trapping model* that will be described later) to the monoclinic fraction of the nanoparticles measured when cooling from 1450 K. Recreated figure with permission from M. Forker *et al.*, Phys. Rev. B 77, 54108 (2008) [123]. Copyright 2008 by the American Physical Society.

The most remarkable aspect of the data in Figs. 15 and 16 is the pronounced decrease of the monoclinic fraction f upon cooling. When continuously lowering the temperature from T < 1500 K, f remains constant down to T~700 K, and then drops by about 35% within a temperature interval of 150–200 K. The frequency distribution of the remaining monoclinic component, however, maintains the narrow line width δ reached at T~1500 K. The reduction of the monoclinic intensity f observed for the nanoparticles indicates that below T~700 K, a large fraction of the probe nuclei in these particles becomes subjected to a different QI. As in the native coarse-grained oxides, this second component (in the following termed "defect" component) mainly shows up as a pronounced loss of anisotropy in the first few nanoseconds. Again, at larger delay times, the PAC pattern contains no other oscillatory components than those of the monoclinic oxide.
It is important to stress that the appearance of this defect component, which has been found for all nanoparticles, bare, coated, and outgassed, in powder samples and pellets and for all precursors, is fully reversible: Upon cooling from T> 1200 K, the monoclinic fraction drops to f_m ~0.65 at T<500 K, but by heating to T>800 K, its saturation value f_m ~0.95 is promptly restored.

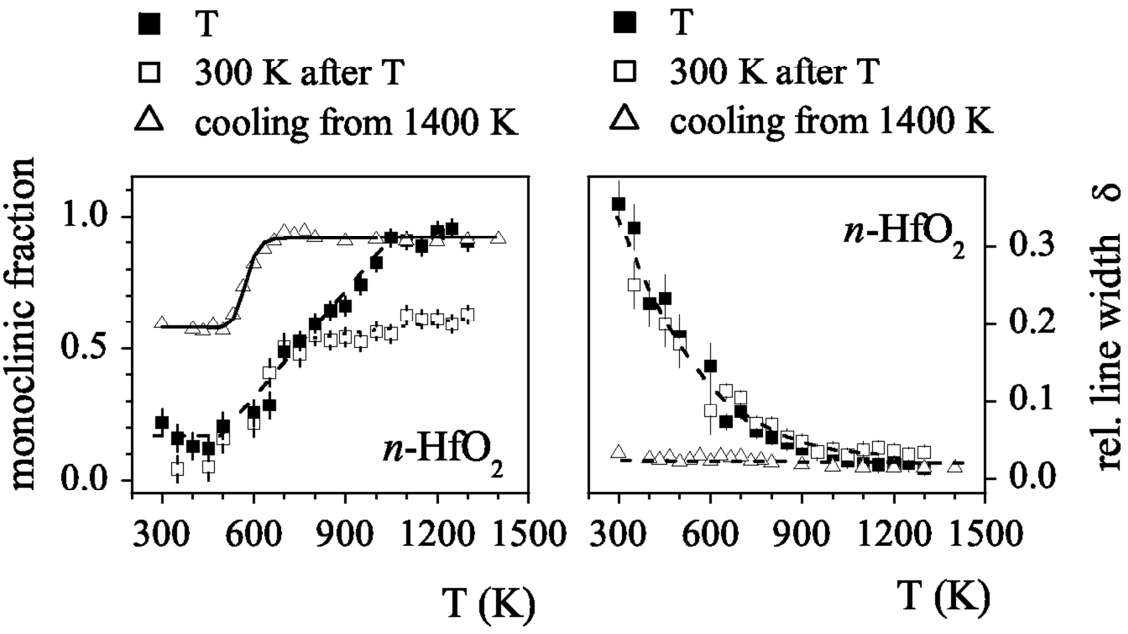

Fig. 16: The monoclinic fraction and the line-width of the QI of ^{181}Ta in nanoparticles of HfO_2 as a function of temperature. The powder samples (in vacuum) were cycled between T (full squares) and 300 K (open squares), and at the end, continuously cooled from 1400 K. The solid lines represent fits (*two trapping model*) to the monoclinic fraction measured upon cooling from 1400 K. Recreated figure with permission from M. Forker *et al.*, Phys. Rev. B 77, 54108 (2008) [123]. Copyright 2008 by the American Physical Society.

The reversible appearance of a defect component at the expense of the monoclinic fraction upon cooling was also observed when the nanoparticles were cycled between an elevated temperature T and 300 K. The effect is easily seen in Fig. 16, where from T~700 K onwards, f(300 K) is significantly smaller than f(T), while δ(300 K) ≈ δ(T). Cooling from 1300 to 300 K results in a pronounced loss of amplitude; the attenuation of the oscillations with time, however, is not affected. The difference [f(1400 K) - f(300 K)] was found to be independent of the time (within 100 h) the sample was kept at 1400 K. Due to the lack of oscillatory structure of the defect component, the precision of its QI parameters is as limited as that of component II of the cg-oxides. Assuming a static QI distribution, one obtains QI parameters of the order ν_Q ~ 1100–1300 MHz, η ~ 0.3–0.5, and δ ~ 0.4–0.6, which are quite similar to those of component II of the coarse grained oxides already described.

The data of cg-HfO_2 in Fig. 15, illustrate that the bulk material presents a different behavior: Here, the monoclinic fraction maintains its high-temperature value upon cooling. Note: cg-HfO2 was cycled between T and 300 K, and the plot in Fig. 15 shows at a given T both the monoclinic fraction f(T) measured at this temperature and the fraction f(300 K) observed at 300 K after cooling from T. One finds f(300 K) = f(T) at all T. Obviously, the appearance of the defect component in the ^{181}Ta PAC spectra is correlated to the particle size. The same particle size effect has been observed in the ^{181}Ta PAC study of n-ZrO_2 particles synthesized by gas phase condensation [126]. In that PAC experiment the sample was annealed at increasing temperatures T_A and, after each annealing step, the ^{181}Ta PAC was measured at room temperature. For grain sizes d~50 nm (determined by XRD), the monoclinic fraction f(290 K) remained far below the saturation value: f(290 K) < 0.6. However, when d exceeded 100 nm at T_A~1400 K, the monoclinic fraction saturated at f(290 K) ~1, i.e., the defect component had disappeared. At 1450 K, the grain size of the particles studied in the recent investigation of Forker *et al*. does not exceed d ~30 nm and, in these particles, about one-third of the probe nuclei are subject to the defect interaction upon cooling below T~700 K. The comparison of the previous [126] and the recent PAC experiments then suggest a critical grain diameter d~100 nm for the appearance of the defect component.

Finally, it is worth mentioning that the ^{181}Ta QI parameters ν_Q and η of HfO_2 nanoparticles, bare or coated, at different temperatures agree, within the experimental accuracy, with those of the coarse-grained material. Also, it is noteworthy that upon heating, the disordered component II in the PAC spectra of the coarse-grained material vanishes, irreversibly, in the same temperature range as the reversible defect component of the nanocrystalline oxides (see Fig. 15), which—together with the similarity of their QI parameters – suggests that in both cases one observes the dissolution of the same defect.

In order to obtain more information on the mechanism that leads to the appearance of the defect component in the ^{181}Ta PAC spectra of the nanocrystalline oxides at T~700 K, it appeared of interest to broaden the investigation of QIs in nanocrystalline oxides to other probe nuclei. Forker *et al*. choose the other popular PAC probe: ^{111}Cd. Sample preparation, therefore, requires doping of the nanoparticles with radioactive ^{111}In. Forker *et al.* prepared the samples by ion implantation of ^{111}In at 160 keV into pellets of n-HfO_2 compacted with 0.4 GPa. The implantation was carried out at the isotope separator of HISKP/Bonn[a]. After implantation, the samples were annealed enclosed in fused silica tubes, in a tube furnace at 1200 K for 10–20 h. The PAC spectra observed after this heat treatment require as much as four components with different QIs to reproduce the spectra over the entire temperature range. The component that dominates at all temperatures (decreasing reversibly from f_1 ~0.7 at 300 K to f_1 ~0.6 at 1200 K) is characterized by a broad distribution of strong QIs. This fraction corresponds to probes implanted in the interfacial regions between the nanoparticles. In addition, three components with sharp frequencies are found. The QI parameters of all the sharp components are very close to those observed by Luthin *et al.* [127] in the coarse-grained oxide. One

a Helmholtz Institut für Strahlen-und Kernphysik, Universität Bonn, Germany.

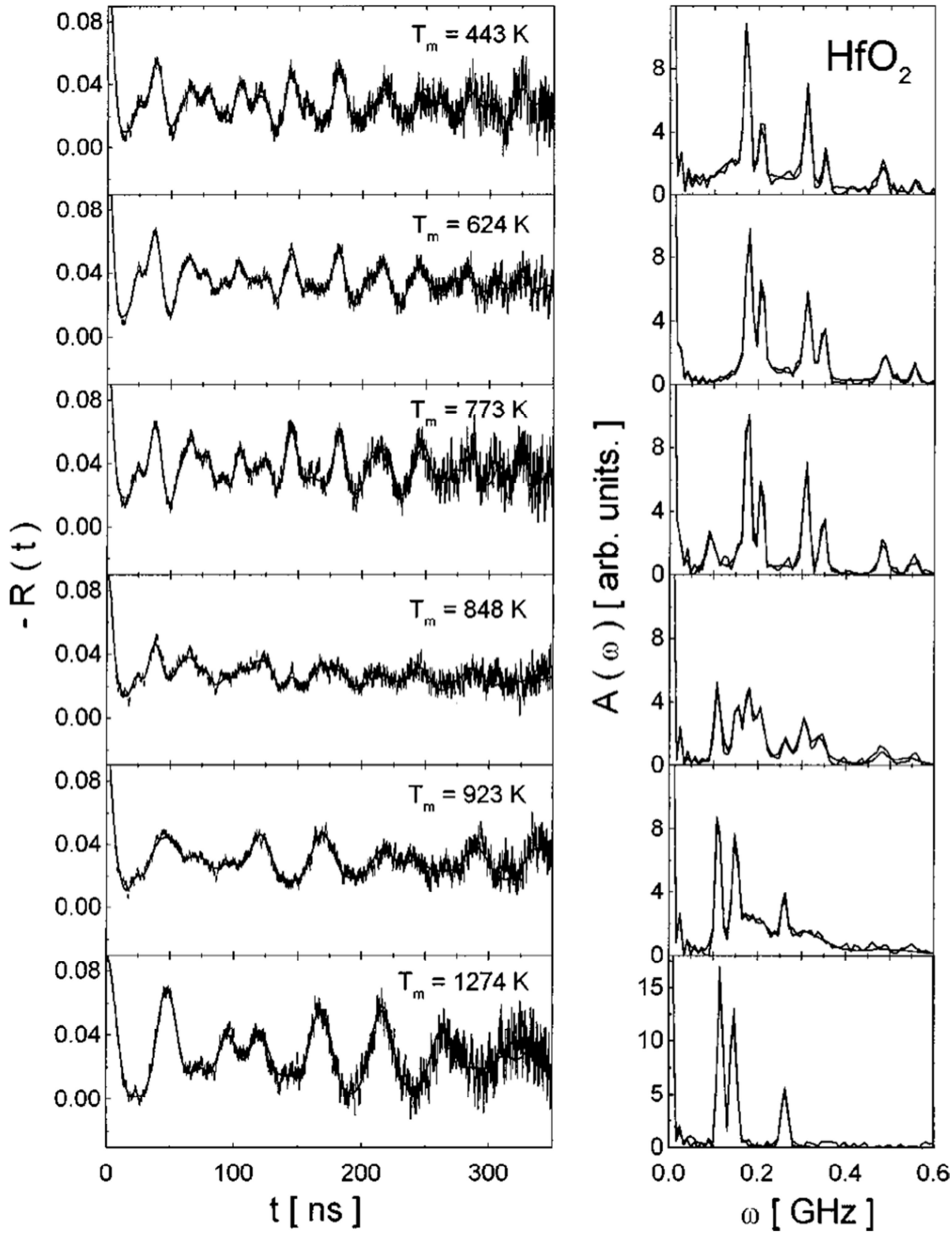

Fig. 17: PAC spectra and their Fourier transforms for ^{111}Cd in HfO_2 measured at 443-1274 K in air. Reprinted figure with permission from J. Luthin *et al.*, Phys. Rev. B 57, 15272 (1998) [127]. Copyright 1998 by the American Physical Society.

of the components has been identified by Luthin *et al.* as ^{111}Cd on substitutional sites of monoclinic HfO_2. The other two remained components have been associated with different charge states of oxygen neighbors of the ^{111}Cd probes caused by the trapping of electron holes. The difference between the results obtained in the experiments carried out by Forker *et al*. and Luthin *et al*. suggests that in the nanoparticles only 50% of the implanted probes end up on regular host sites. PAC results obtained by Luthin *et al.* on cg-HfO_2 are shown in Figure 17. The complex structure of the spectra is produced by the coexistence of the three sharp QI components mentioned above.
In this chapter, we will take into account only the relative intensities f of ^{111}Cd at substitutional sites of monoclinic n-HfO_2 (normalized to f (T)~1 at T>1200 K) at different temperatures that are collected in Fig. 18 (full triangles), which for comparison includes the temperature dependence of the monoclinic fraction of the probe ^{181}Ta in the same nanoparticles and of both ^{111}Cd and ^{181}Ta in the corresponding coarse–grained oxide.
It is an important observation that for the two probes, ^{181}Ta and ^{111}Cd, the temperature dependence of the monoclinic fraction f(T) differs substantially. This indicates that probe rather than host properties must play the decisive role in the reversible appearance of nanoparticle defect components upon cooling from T<1200 K. The main differences are the following:
The decrease of f(T) for the two probes extends over different temperature ranges.
In the case of ^{181}Ta, there is clear evidence for a particle size effect.
In the case of ^{111}Cd, the temperature dependence of the monoclinic fraction is independent of the particle size. All ^{111}Cd probes are affected by the defect formation, both in nanocrystalline and coarse-grained oxides.

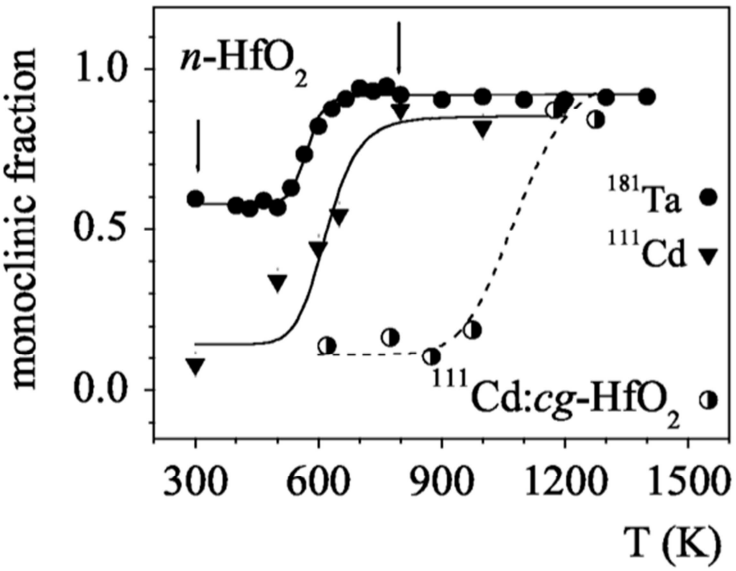

Fig. 18:The fraction of the probe nuclei ^{181}Ta and ^{111}Cd located at substitutional sites of monoclinic hafnia nanoparticles as a function of temperature. The solid and dashed lines are fits of Eqs. (5) and (6) to the experimental data. The arrows mark the temperature range used in the analysis of the ^{181}Ta data. In the case of ^{111}Cd, the entire temperature range T<1200 K was taken into account. For comparison, the fraction of ^{111}Cd at substitutional sites of coarse-grained monoclinic HfO_2 (taken from Ref. 127) is included. Recreated figure with permission from M. Forker *et al.*, Phys. Rev. B 77, 54108 (2008) [123]. Copyright 2008 by the American Physical Society.

It appears improbable that the appearance of the defect component in the ^{181}Ta PAC spectra reflects structural defects of the host oxides. The nanoparticles annealed at T_A>1200 K show a high degree of order; their PAC spectra are practically identical to those of the coarse-grained oxides. The formation of structural defects upon cooling would, therefore, require the diffusion of cations and/or oxygen ions.

Using the diffusion parameters of oxygen in nanocrystalline zirconia [128], Forker *et al.* estimate oxygen jump rates [129] of the order of 10^{-4} and 10^{-1} s^{-1} for the core and the interfacial region, respectively, of nanocrystalline ZrO_2 at T~600 K, where the defect component starts to appear. The cation jump rates are even smaller. Forker *et al*., therefore, discard – on the time scale of the PAC experiment – the possibility of atomic diffusion at T<700 K and, hence, exclude structural defects as an explanation for the defect component.

Diffusionless structural transformation is also unlikely. In such a case, one would expect another static QI of possibly different symmetry and strength but narrow line width, and the thermal evolution of this component would not extend over a temperature range of the order of 150–200 K. Excluding structural defects or transformations, the formation of electronic defects involving the probe atom should be considered as possible explanation of the defect component.

The fact that the monoclinic fractions as seen by ^{181}Ta and ^{111}Cd, respectively, have completely different temperature dependencies f (T) and the absence of a particle size effect in the case of ^{111}Cd (Fig. 18) point into this direction. An important difference between these probes concerns their charge state in HfO_2. After the ^{111}In→^{111}Cd electron-capture decay, ^{111}Cd has valence 2+ and, in a lattice of tetravalent Hf ions, is attractive to positive charge carriers. Based on cluster calculations of the EFG, Luthin *et al.* [127] have attributed the observed reversible change of population of the components f_i, and f to thermal trapping and detrapping of one or two positive electron holes at nearest oxygen neighbors of the probes. Cation vacancies are considered, by charge neutrality arguments, as the source of these electron holes. ^{181}Ta produced by the β^- decay of ^{181}Hf, on the other hand, has nominal valence 5+. Relative to tetravalent Hf, ^{181}Ta thus constitutes a positively charged impurity and it is conceivable that at low temperatures electrons are trapped by these impurity states, forming neutral Ta-electron configurations with a different QI at the nuclear site. Casali *et al*. [130] had reported *ab initio* calculations of the EFG at Ta nuclei on substitutional Hf sites of monoclinic HfO_2 for the Ta charge states Ta^+ and Ta^0. According to these calculations, the quadrupole frequency ν_q and asymmetry parameter η for the charge state Ta^0 should be about 20% larger than for Ta^+. The difference of the experimental QI parameters of the monoclinic phase ν_q ~800 MHz and η~0.34 and the defect component (ν_q ~1100–1200 MHz, η~0.2–0.4, and δ ~ 0.4 – 0.6) in the nanocrystalline oxides is of this order of magnitude (50%). More recently, in a detailed *ab initio* study were the dilution of the Ta impurities was increase and showed to be crucial for the EFG predictions [131], gives a 55% difference between the EFG for Ta^o and Ta^+, in excellent agreement with the experiments.

Within the framework of this interpretation, the pronounced line broadening of the defect component – attributable to either a static QI distribution or slow QI fluctuations – requires the existence of several trapping sites. A static occupation of nonequivalent sites would produce a QI distribution; electrons slowly hopping between equivalent sites would lead to QI fluctuations.

The proposed electron trapping is described in a two state model where mobile electrons are either in the conduction band at E=0 or occupy the Ta^+ states at E = $-E_d$. The relative intensity of the defect component in thermal equilibrium, i.e., the fraction of probe nuclei decorated with a trapped electron, f_d, is then given by [Maxwell–Boltzmann distribution with degeneracies c_P and $(1 - c_P)$, c_P = relative probe concentration]

$$f_d(T) = f_o \frac{1}{\left[1 + \left(1/c_p - 1\right)\exp\left(-E_d / k_B T\right)\right]} \qquad [5]$$

with f_0=1 for c_e>c_p, and f_0=c_e/c_p for c_e<c_p, where c_p and c_e are the probe and electron concentrations, respectively. The fraction f(T) of probes in the monoclinic phase without a trapped electron is then:

$$f(T) = \left[1 - f_V f_d(T)\right] \qquad [6]$$

The parameter f_V is a measure of the volume fraction where electrons are available for trapping. Fit of this equation to the f (T) data of Figs. 15 and 16 lead to Ta-electron binding energies of E_d ~0.90(15) eV for nanocrystalline hafnia and a probe concentration ratio c_p (probes per total number of metal ions) between 10^{-6} and $10^{-8.}$ The relatively large uncertainties of c_p and E_d are a consequence of the strong correlation of these parameters in the above equations. Assuming that the number of mobile electrons available exceeds the number of probes (c_e>c_p, i.e., f_0=1), Forker *et al*. obtain f_V ~0.35–0.4. The value of c_p deduced from f(T) in Figs. 15 and 16 is in good agreement with the probe concentration estimated from the γ -ray intensity of the PAC source. The total number of ^{181}Ta probes of a typical PAC source is of the order of 10^{12} atoms which, for oxide samples of a few milligrams, correspond to a probe concentration c_p~10^{-7}. The proposed interpretation of the defects as Ta probes with a trapped electron requires a total of 10^{11}–10^{12} mobile electrons. One possible electron source are positively charged oxygen vacancies. To account for the experimentally observed size effect (f_V ~0.35–0.4 at grain diameter d ~25–30 nm, and f_V ~0 at d>100 nm), these would have to be concentrated—in the case of a spherical particle—in a surface layer of ~3.5 nm thickness. A conceivable mechanism for such concentration has been mentioned by Shukla and Seal [132] in a discussion of the "nanoparticle size effect": In nanocrystalline powders with an important fraction of the atoms residing near the surface, a large number of metal oxygen bonds may be weakened, resulting in the desorption of oxygen ions and the creation of oxygen vacancies in the surface region. On the other hand, Kang *et al*. [133] have shown that defect complexes consisting of oxygen vacancies and hydrogen (V_O-H) behave as shallow donors. Forker *et al*. assumed such complexes probably exist in the surface region of the nanoparticles. Indeed, they observed, using nuclear magnetic resonance, that after heating to high temperatures there is a hydrogen concentration in the range of 2.5–5.0 wt%. It may, hence, be assumed that the nanoparticles of the encapsulated PAC sources still carry a sizable hydrate layer when they are cooled from high temperatures. (V_O-H) complexes at the interface of nanoparticles and their hydrate layers may, therefore, constitute another possible source of the electrons required by the Ta^+ trapping model.

As it was already pointed out, upon heating, the disordered component II in the PAC spectra of the coarse-grained material vanishes, irreversibly, in the same temperature range as the reversible defect component of the nanocrystalline oxides (see Fig. 15), which suggests that in both cases one observes the dissolution of the same defect. Forker *et al*. explain this behavior assuming that coarse-grained oxides may contain some disorder in the native state and a certain fraction of neutral Ta-electron (Ta^0) complexes is possibly formed. Upon heating, these complexes become ionized and the disordered fraction vanishes. However, with increasing temperature, the oxygen vacancies also migrate toward grain-boundary sinks and, as the fraction of Ta probes in the grain-boundary volume of coarse-grained particles is very small, the disordered component in the PAC spectra of cg-HfO_2 does not reappear upon cooling.

The same trapping model involving positive electron holes rather than electrons may be used to describe the reversible temperature dependence of the monoclinic fraction of $^{111}Cd^{2+}$ in nanocrystalline and coarse-grained HfO_2 (see Fig.16) [127]. In contrast to ^{181}Ta, in the case of ^{111}Cd, the monoclinic fraction – both in bulk and nanocrystalline oxides – disappears completely upon cooling. This absence of a size effect means that all probe atoms participate in hole trapping and detrapping, and implies a homogeneous distribution of electron holes throughout the samples. For HfO_2, the data presently available suggest an influence of the particle size on the binding energy. For ^{111}Cd in bulk and nanocrystalline HfO_2, one obtains E_d=1.5 (2) eV and E_d=0.85(2) eV, respectively.

Summary

In this chapter PAC determinations of the hyperfine interactions at impurity sites in binary oxides have been presented. Many of these oxides have important technological applications and often the relevant physical properties are determined by the quality and quantity of the impurities or defects in the oxides.
References to very interesting investigations on HfO_2, In_2O_3, La_2O_3, TiO_2 were given. Experiments carried out on HfO_2 and In_2O_3, doped with ^{111}In (EC) ^{111}Cd and ^{181}Hf (β^-) ^{181}Ta were extensively described. In these examples, the complementary use of both probes allows to conclude on the role of the probe in the observed effects. In the appendix, tables with all the published data, using the mentioned probes in binary oxides, are presented.
Generally, the PAC observations at the impurity centers can be related to the physical properties of the host, at least in a qualitative way. State-of-the-art *ab initio* calculations appear now as a powerful complementary tool in this kind of studies, necessary to obtain the physical information involved in impurity-host systems with precision and reliability.
Important space of the chapter has been dedicated to the *after-effects* following the electron-capture decay of ^{111}In. This isotope forms the source of the highly ionized impurity center through the electron-capture radioactive decay, and at the same time gives place to the nuclear probe ^{111}Cd in the PAC measurements. The PAC observation is sensitive to the total availability of electrons at the impurity center. The applicability of the PAC technique in this sense was announced 25 years ago by Bibiloni *et al.* [10] and, since then, this possibility has been tested in several cases. A theoretical approach, which accounts for these observations in terms of impurity levels, conductivity, electron concentration, and so on, is still missing.

Acknowledgements

We have the pleasure to gratefully acknowledge Prof. Dr. K.P. Lieb (II. Physikalisches Institut, Universität Göttingen) and Prof. Dr. M. Forker (HISKP, Universität Bonn) for giving permission to reproduce and/or recreate several figures from their articles, giving access to some of their original data. We are indebted to Lic. E.L. Muñoz (UNLP) for giving permission to show unpublished data and for his assistance during the construction of the Appendix.

Appendix

Table I: Hyperfine parameters of PAC measurements in binary oxides using ^{111}In(EC)^{111}Cd as probe. When ^{111m}Cd was also used, this is explicitly indicated but the ^{111}In value is the only reported, as V_{33} and η values are the same for both probes. The oxides are grouped according to their cation coordination geometry.

Oxide Host	Fraction (%)	V_{33} [10^{21} V/m^2]	η	Comments	Refs.
A-La_2O_3		13.9(1)	0.10(1)	Value extrapolated to RT, due to the presence of ECAE. In the 2nd quoted Ref., this highly distributed EFG is measured at RT	13,134
A-Nd_2O_3		13.4(1)	0.09(1)		133
α-Al_2O_3		10.9(1)	0.00	Singlecrystals, with ^{111m}Cd and ^{111}Cd, ECAE only present in the last case, V_{33} in [001]	134
		10.91(5)	0.00	Singlecrystals	12
α-Cr_2O_3	73	7.4(1)	0.00		136
		10.06(5)	0.00	T_m= RT, assigned to Cd^0. In agreement with ab initio calculations by Ref. [37].	19
		7.52 (5)	0.00	T_m=1370 K. assigned to Cd^{-1}. In agreement with ab initio calculations by Ref. [37].	19
α-Fe_2O_3		8.1(6)	0.00	T_m=RT, T_{Neel}=959 K. Very reliable.	137
α-Ga_2O_3	2(2)	9.07(9)	0.00	T_m=RT.	14
	31(2)	8.97(5)	0.00	T_m=723 K	14
α-Rh_2O_3		6.83(4)	0.00	T_m=RT , extrapolated for $\delta\omega_Q$-->0	138
α-V_2O_3		6.57(2)	0.00	T_m=296 K, transforms to m-V_2O_3 below T_t=160 K	139
m-V_2O_3		8.09(3)	0.00	T_m=148 K, antiferromagnetic	139
β-Fe_2O_3 (C)	77	8.22(5)	0.62(2)		140
(D)	23	9.12(5)	0.05(2)		140
β-Mn_2O_3 (C)		10.36(5)	0.68(1)		140
(D)		5.76(3)	0.11(2)		140
C-Sc_2O_3 (C)		6.50(5)	0.71(1)	Additional HFI3 seen, with $(f_C+f_3)/f_D\approx3$. Presence of ECAE. ^{111}In was implanted.	64
(D)		8.27(9)	0.00	Additional HFI3 seen, with $(f_C+f_3)/f_D\approx3$. Presence of ECAE. ^{111}In was implanted.	64
C-In_2O_3 (C)		5.8(3)	0.70(1)	T_m=RT, T_{range}= 14-1073 K, presence of ECAE, time range 200 ns	10
(D)		7.8(4)	0.12(4)	T_m=RT, T_{range}= 14-1073 K, presence of ECAE, time range 200 ns	10
(C)		5.9(1)	0.69(5)	In_2O_3 thin film over Al substrate, removal of the ECAE. Time range 400 ns	100
(D)		7.7(1)	0.00(5)	In_2O_3 thin film over Al substrate, removal of the ECAE. Time range 400 ns	100
(C)	77	5.93(2)	0.71(1)	T_m=873 K. Presence of ECAE	88
(D)	23	7.73(2)	0.00	T_m=873 K. Presence of ECAE	88
C-Lu_2O_3 (C)		2.90(2)	1.0	T_m=300 K, agrees with APW+lo Cd^0	17,18
(C)		4.91(2)	0.764(7)	T_m=1273 K, agrees with APW+lo Cd^{1-}	17,18
(D)		7.76(3)	0.04(4)	T_m=300 K, agrees with APW+lo Cd^0	17,18

Table I (cont.)

(D)		7.90(3)	0.00(6)	T_m=1273 K, agrees with APW+lo Cd^{1-}	17,18
(C)		2.93	0.78	T_m=973K. Strongly damped below T_m=600 K.	141
(D)		7.48	0.00	T_m=973 K. Strongly damped below T_m=600 K.	141
C-Yb_2O_3 (C)		4.83(5)	0.75(2)	Additional HFI3 seen, with $(f_C+f_3)/f_D\approx3$. Presence of ECAE in a low % of probes.	64
(D)		7.67(9)	0.00	Additional HFI3 seen, with $(f_C+f_3)/f_D\approx3$. Presence of ECAE in a low % of probes.	64
C-Tm_2O_3 (C)		3.47	0.72	T_m=600 K. Strongly damped below T_m=600 K.	141
(D)		7.89	0.0	T_m=600 K. Strongly damped below T_m=600 K.	141
C-Tl_2O_3 (C)		6.49	0.21	T_m=295 K	141
(D)		6.65	0.0	T_m=295 K	141
C-Er_2O_3 (C)		4.25(3)	0.97(3)	Additional HFI3 seen, with $(f_C+f_3)/f_D\approx3$. ECAE are not present.	142
(D)		7.36(3)	0.00	Additional HFI3 seen, with $(f_C+f_3)/f_D\approx3$. ECAE are not present.	142
C-Y_2O_3 (C)		4.43(9)	0.77(2)	Additional HFI3 seen, with $(f_C+f_3)/f_D\approx3$. Presence of ECAE.	64
(D)		7.47(9)	0.00	Additional HFI3 seen, with $(f_C+f_3)/f_D\approx3$. Presence of ECAE.	64
C-Ho_2O_3 (C)		4.05(5)	0.83(2)	Additional HFI3 seen, with $(f_C+f_3)/f_D\approx3$. ECAE are not present.	143
(D)		7.47(9)	0.00	Additional HFI3 seen, with $(f_C+f_3)/f_D\approx3$. ECAE are not present.	143
C-Dy_2O_3 (C)		4.08(9)	0.81(5)	Additional HFI3 seen, with $(f_C+f_3)/f_D\approx3$. ECAE are not present.	64
(D)		7.42(9)	0.00	Additional HFI3 seen, with $(f_C+f_3)/f_D\approx3$. ECAE are not present.	64
C-Gd_2O_3 (C)		3.1(1)	0.97(3)	Additional HFI3 seen, with $(f_C+f_3)/f_D\approx3$. ECAE are not present.	143
(D)		7.2(2)	0.00	Additional HFI3 seen, with $(f_C+f_3)/f_D\approx3$. ECAE are not present.	143
C-Eu_2O_3 (C)		3.90(3)	0.90	Additional HFI3 seen, with $(f_C+f_3)/f_D\approx3$. ECAE are not present.	142
(D)		8.43(3)	0.00	Additional HFI3 seen, with $(f_C+f_3)/f_D\approx3$. ECAE are not present.	142
(C)		2.154	0.87	T_m=565 K	141
(D)		7.249	0.00	T_m=565 K	141
C-Sm_2O_3 (C)		2.93(9)	0.91(3)	Additional HFI3 seen, with $(f_C+f_3)/f_D\approx3$. ECAE are not present.	143
(D)		7.17(5)	0.07(5)	Additional HFI3 seen, with $(f_C+f_3)/f_D\approx3$. ECAE are not present.	143
CdO		0.0		T_m=RT-770 K. Very broad EFG distribution around V_{33}=0. ECAE are not present	144
NiO		0.0		T_C=631 K ; T_m=700 K and 295 K ; T_N=550 K	145
NbO_2 (1)	47	10.0(1)	0.36		146
(2)	41	6.5(1)	0.85		146
SnO_2		5.78(5)	0.1(1)	Fraction increases from 25% at 4 K to 70 % at 1000 K, due to the presence of ECAE.	15
		5.83(4)	0.18(2)	T_m=293 K	105
TiO_2		5.23(5)	0.18(1)	T_m=293 K	104
		5.34(2)	0.18(1)	T_m=290 K	20

Table I (cont.)

		5.34(2)	0.18(1)	Singlecrystal , T_m=290 K , V_{33} in [110] (=[-1 1 0])	26
Mn_3O_4(B)		9.32(5)	0.89(1)	Octahedral site. As assigned in Ref. 147.	140
		4.32(2)	0.13(6)	As assigned in Ref. 140. At least difficult to decide.	140
β-Ga_2O_3(2)	69(1)	5.934(5)	0.13(1)	Octahedral site, preferential occupation, T_m=863 K	14
MoO_3		2.1(3)	0.2	η not well defined, obtained through χ^2 test	148
Co_3O_4(B)		7.27(4)	<0.07	Octahedral site	149
Mn_3O_4(A)		4.32(2)	0.13(6)	Tetrahedral site. As assigned in Ref. 147.	140
		9.32(5)	0.89(1)	Tetrahedral site. As assigned in Ref. 140. At least difficult to decide.	140
ZnO		1.555(5)	0.00	Poly and singlecrystalline samples, V_{33} in [001]	15
		1.7(3)	0.00	Error in V_{33} takes into account the Q error	73
	85	1.584(5)	0.00	ZnO commercially obtained (99.99% purity)	150
	100	1.569(1)	0.00	ZnO prepared by the sol-gel method	150
Co_3O_4 (A)		0.0(2)		Regular tetrahedral site	149
β-Ga_2O_3 (1)	20(1)	9.17(5)	0.32(6)	Tetrahedral site, T_m=863 K	14
SnO	80	5.7(9)	0.18(1)	T_m=RT. Assigned (via APW calculations) to Cd^0 charge state. At higher temperatures V_{33} is better defined. Presence of ECAE.	16
	20	8(1)	0.44(2)	T_m=RT. Assigned (via APW calculations) to Cd^{1+} charge state (trapped hole). At higher temperatures V_{33} is better defined. Presence of ECAE.	16
AgO		16.1(2)	0.0(1)		100
CuO		20.93(4)	0.42(1)	Very reliable	151
Ag_2O		6.4(4)	0.00(5)		100
Cu_2O		6.18(4)	0.00	Very reliable, from ^{111}In implantation in polycrystalline Cu_2O and from reduced ^{111}In-implanted CuO.	151
		4.2(2)	0.7(1)	HFI seen in oxidized Cu:^{111}In samples, assigned in Ref. 150 to Cu sites with defects in Cu_2O.	152
B-Sm_2O_3		10.31(1)	0.979(5)	Only one site populated among 3 possible cation sites. Assigned to site Sm(3) in Ref 154.	153
B-Eu_2O_3		10.36(5)	0.975(8)	Only one site populated among 3 possible cation sites. Assigned to site Sm(3) in Ref 154.	153
B-Gd_2O_3		10.40(2)	1.00	Only one site populated among 3 possible cation sites. Assigned to site Sm(3) in Ref 154.	153

Table II: Hyperfine parameters of PAC measurements in binary oxides using $^{181}Hf(\beta^-)^{181}Ta$ as probe. The oxides are grouped according to their cation coordination geometry.

Oxide host	Fraction [%]	V_{33} [10^{21} V/m^2]	η	Comments	Refs.
α-Al_2O_3		11.0(2)	0.17(3)	Singlecrystal , V_{33} in [001]	155
α-Cr_2O_3					36
α-Fe_2O_3		7.53(2)	0.06(1)	Polycrystalline , T_m=954 K, T_N=955 K	156
		7.5(1)	0.04(4)	Singlecrystal, T_m= 973 K , V_{33} in [001]	37,157
C-Sc_2O_3 (C)	78(2)	14.12(7)	1,00	Fractions normalized for 90% of the probes	93
(D)	22(2)	17.86(3)	0.16(1)	Fractions normalized for 90% of the probes	93
C-In_2O_3 (C)		12.4(1)	0.6(1)	Mean value from 3 samples (films and chemical preparation), 4 HFI present . Inverted fractions, $f_C/f_D < 1$	91
(D)		16.35(2)	0.15(1)	Mean value from 3 samples (films and chemical preparation), 4 HFI present. Inverted fractions, $f_C/f_D < 1$	91
(C)	77(2)	16.68(3)	0.154(4)	New experiment, supported by ab initio calculations	35
(D)	23(1)	18.99(3)	0.02(6)	New experiment, supported by ab initio calculations	35
C-Lu_2O_3 (C)	80(3)	13.96	0.452(4)	T_m=300 K	92
(D)	20(1)	23.55	0.06(4)	T_m=300 K	92
C-Yb_2O_3 (C)	65(5)	13.68(6)	0.47(1)		94
(D)	35(5)	23.32(2)	0.01(4)		94
C-Tm_2O_3 (C)	66(8)	13.16(9)	0.49(1)	Doped by ball milling-assisted solid-state reaction	96
(D)	34(8)	22.5(1)	0.00	Doped by ball milling-assisted solid-state reaction	96
C-Er_2O_3 (C)	69(2)	12.9(6)	0.570(6)	Fractions normalized for 90% of the probes	95
(D)	31(2)	22.73(9)	0.00	Fractions normalized for 90% of the probes	95
C-Y_2O_3 (C)	70(6)	13.06(3)	0.544(3)		94
(D)	30(3)	22.86(7)	0.00		94
C-Ho_2O_3 (C)	70(4)	12.76(3)	0.612(4)	T_m=300 K, normalized fractions for 80% of probes, 2 more minor fractions at T_m<573 K	29
(D)	30(5)	23.09(8)	0.00	T_m=300 K , normalized fractions for 80% of probes, 2 more minor fractions at T_m<573 K	29
C-Dy_2O_3 (C)	69(5)	11.9(1)	0.649(7)		94
(D)	31(5)	21.77(1)	0.0(2)		94
C-Gd_2O_3 (C)	74(3)	11.80(3)	0.768(4)	Fractions normalized for 70% of probes	95
(D)	26(1)	22.08(6)	0.00	Fractions normalized for 70% of probes	95
C-Eu_2O_3 (C)	74(8)	11.37(3)	0.798(4)	T_m=300 K	29
(D)	26(3)	21.6(1)	0.00	T_m=300 K	29
C-Sm_2O_3 (C)	63(9)	11.9(2)	0.81(4)	T_m=300 K, 15% of the monoclinic the B-Sm_2O_3 phase	92
(D)	22(8)	21.3(2)	0.00	T_m=300 K, 15% of the monoclinic the B-Sm_2O_3 phase	92
SnO		12.98(4)	0.07(2)	Polycrystals	101
SnO_2		17.02(4)	0.72(1)	SnO_2 crystalline thin film	101
		16.96(4)	0.7	^{181}Hf-doped Sn-O thin film and then crystallized	102

Table II (cont.)

TiO_2	100	14.32(7)	0.55(1)	Singlecrystal, V_{33} in [001]	30
		14.19(6)	0.57(1)	Polycrystal, T_m=0 K, extrapolated	20
β-Ga_2O_3(2)	30		0.40(1)	δ=2(1) %. Invoked for the octahedral site. Singlecrystals, V_{33} normal to the a-b plane	158
ZnO		3.77(4)	0.04(10)	Polycrystalline pellet	159
β-Ga_2O_3(1)	-	-	-	Not seen…	158
m-ZrO_2		14.2(5)	0.335(15)	T_m=RT ?	114
	80	14.05(4)	0.335(5)	T_m=300 K	123
m-HfO_2	75	13.90(4)	0.345(5)	T_m=300 K	123
	70	13.72(6)	0.340(3)	T_m=300 K	120
	87	13.8(1)	0.35(1)	T_m=RT	160
	100	13.85(6)	0.378(4)	T_m=RT	32
	100	14.01(9)	0.354(5)	T_m=RT, after 1h at 1273 K treatment in air	96
B-Sm_2O_3 (1)	13(2)	7.65(7)	1.00	T_m=290 K, from transformation of ^{181}Hf-implanted C-Sm_2O_3 bixbyite (this agrees with implantation in the B-phase)	154
(2)	79(3)	17.03(3)	0.619(3)	T_m=290 K, from transformation of ^{181}Hf-implanted C-Sm_2O_3 bixbyite (this agrees with implantation in the B-phase)	154
(3)	8(1)	21.2(2)	0.94(2)	T_m=290 K, from transformation of ^{181}Hf-implanted C-Sm_2O_3 bixbyite (this agrees with implantation in the B-phase)	154
B-Eu_2O_3 (1)	20(2)	14.3(2)	1.00	From transformation of ^{181}Hf-doped C-Eu_2O_3 bixbyite (this agrees with implantation in the B-phase)	161
(2)	70(3)	17.55(7)	0.632(5)	From transformation of ^{181}Hf-doped C-Eu_2O_3 bixbyite (this agrees with implantation in the B-phase)	161
(3)	10(1)	19.0(1)	1.00	From transformation of ^{181}Hf-doped C-Eu_2O_3 bixbyite (this agrees with implantation in the B-phase)	161
B-Gd_2O_3 (1)	13(4)	13.4(3)	0.85(4)	Implantation in the B-Gd_2O_3 phase	161
(2)	78(5)	17.76(3)	0.610(5)	Implantation in the B-Gd_2O_3 phase	161
(3)	9(2)	18.78(9)	1.00	Implantation in the B-Gd_2O_3 phase	161

References

[1] M. Uhrmacher: Physica B Vol. 389 (2007), p. 58.

[2] O. F. Schirmer: J. Phys.: Condens. Matter. Vol. 18 (2006), p. 667.

[3] H. A. Wang, C.H Lee, F.A. Kröger, and R.T. Cox: Phys. Rev. B Vol. 27 (1983), p. 3821.

[4] J. A. Weil: Radiat. Eff. Vol. 26 (1975), p. 261.

[5] W. Hayes and T.J. Jenkin: J. Phys. C: Solid State Phys. Vol. 19 (1986), p. 6211.

[6] H. Seidel and H. C. Wolf, in: *Physics of Color Centers*, edited by W. Beall Fowler, Academic Press, New York (1968).

[7] J. M. Spaeth and F. K. Koschnik: J. Phys. Chem. Solids Vol. 52 (1991), p. 1.

[8] J. M. Spaeth and F. Lohse: J. Phys. Chem. Solids 51 Vol. (1990), p. 861.

[9] J. M. Spaeth , J. R. Niklas, and R.H Bartram: *Structural Analysis of Point Defects in Solids* (Springer, Berlin 1992).

[10] A. G. Bibiloni, J. Desimoni, C. P. Massolo, L. A. Mendoza Zélis, A. F. Pasquevich, F. H. Sánchez, and A. R. López García: Physical Review B Vol. 29 (1984), p. 1109.

[11] A. Lohstroh, M. Uhrmacher, P. J. Wilbrandt, H. Wulff, L. Ziegeler, and K. P. Lieb: Hyperfine Interact. Vol. 159 (2004), p. 35.

[12] J. Penner and R. Vianden: Hyperfine Interact. Vol. 158 (2004), p. 389.

[13] D. Lupascu, S. Habenicht, K. P.Lieb, M. Neubauer, M. Uhrmacher, and T. Wenzel: Phys. Rev. B Vol. 54 (1996), p. 871.

[14] A. F. Pasquevich, M. Uhrmacher, L. Ziegeler, and K. P. Lieb: Phys. Rev. B Vol. 48 (1993), p. 10052; A. F. Pasquevich, Hyperfine Interact. Vol. 60 (1990), p. 791.

[15] H. Wolf, S. Deubler, D. Forkel, H. Foettinger, M. Iwatschenko-Borho, M. Meyer, M. Renn, and W. Witthuhn: Mater. Sci. Forum Vol. 10 (1986), p. 863.

[16] E. L. Muñoz, A. W. Carbonari, L. A. Errico, H. M. Petrilli, and M. Rentería: Hyperfine Interact. Vol. 178 (2007), p. 37.

[17] L. A. Errico, M. Rentería, A. G. Bibiloni, and F. G. Requejo: Hyperfine Interact. Vol. 120/121 (1999), p. 457.

[18] L. A. Errico, M. Rentería, A. G. Bibiloni, and G. N. Darriba: Phys. Stat. Solidi (c) Vol. 2 (2005), p. 3576.

[19] M. Neubauer, A. Bartos, K. P. Lieb, D. Lupascu, M. Uhrmacher, and T. Wenzel: Europhys. Lett. Vol. 29 (1995), p. 175.

[20] J. M. Adams and G. L. Catchen: Phys. Rev. B Vol. 50 (1994), p. 1264.

[21] H. Akai, M. Akai, S. Blügel, B. Drittler, H. Ebert, K. Terakura, R. Zeller, and P. H. Dederichs: Prog. Theor. Phys. Suppl. Vol. 101 (1990), p. 11.

[22] P. Hohenberg and W. Kohn: Phys. Rev. Vol. 136 (1964), p. 864; W. Kohn and L.J. Sham: Phys. Rev. Vol. 140 (1965), p. 1133.

[23] O. K. Andersen: Phys. Rev. B Vol. 12 (1975), p. 3060.

[24] P. Blaha, K. Schwarz, G. K. H. Madsen, D. Kvasnicka and J. Luitz: WIEN2k: An Augmented Plane Wave Plus Local Orbitals Program for Calculating Crystal Properties (Technische Universität, Wien, 2001).

[25] S. Lany, P. Blaha, J. Hamann, V. Ostheimer, H. Wolf, and T. Wichert: Phys. Rev. B Vol. 62 (2000), p. R2259.

[26] L. A. Errico, G. Fabricius, M. Rentería, P. de la Presa, and M. Forker: Phys. Rev. Lett. Vol. 89 (2002), p. 055503.

[27] L. A. Errico, G. Fabricius, and M. Rentería: Phys. Rev. B Vol. 67 (2003), p. 144104.

[28] L. A. Terrazos, H. M. Petrilli, M. Marszalek, H. Saitovich, P. R. J. Silva, P. Blaha, and K. Schwarz: Solid State Commun. Vol. 121 (2002), p. 525.

[29] L. A. Errico, M. Rentería, A. G. Bibiloni, and K. Freitag: Physica B Vol. 389 (2007), p. 124.

[30] G. N. Darriba, L. A. Errico, P. D. Eversheim, G. Fabricius, and M. Rentería: Phys. Rev. B Vol. 79 (2009), p. 115213.

[31] L. A. Errico, M. Rentería, G. Fabricius, and G. N. Darriba: Hyperfine Interact. Vol. 158 (2004), p. 63.

[32] L.A. Errico: PhD Thesis, University of La Plata (UNLP), 2002.

[33] L. A. Errico, G. Fabricius, and M. Rentería: Hyperfine Interact. Vol. 136/137 (2001), p. 749.

[34] L. A. Errico, G. Fabricius, and M. Rentería: Phys. Stat. Solidi B Vol. 241 (2004), p. 2394.

[35] E. L. Muñoz, L. A. Errico, G. N. Darriba, A. G: Bibiloni, P. D. Eversheim and M. Rentería: "*Ab initio* and experimental study of Ta-doped In_2O_3 semiconductor", contribution to the Int. Workshop "At the Frontiers of Condensed Matter Physics III", 11-15 December 2006, Buenos Aires, Argentina. To be published.

[36] G. N. Darriba, L. A. Errico, E. L Muñoz, D. Richard, P. D. Eversheim, and M. Rentería: Physica B Vol. 404 (2009), p. 2739.

[37] G. N. Darriba: PhD Thesis, University of La Plata (UNLP), 2009.

[38] M. C. M. O'Brien: Proc. R. Soc. London, Ser. Vol. 231 (1955), p. 404.

[39] J. Schneider and O.F. Schirmer: Z. Naturforsch. Vol. 18a (1963), p. 20.

[40] A. M. Stoneham, J. Gavartin, A.L. Shluger, A. V. Kimmel, D. Muñoz Ramo, H. M. Rønnow, G. Aeppli, and C. Renner: J. Phys.: Condens. Matter Vol. 19 (2007), p. 255208.

[41] G. Pacchioni, F. Frigoli, D. Ricci, and J. A. Weil: Phys. Rev. B Vol. 63 (2000), p. 54102.

[42] J. Lægsgaard and K. Stokbro: Phys. Rev. Lett. Vol. 86 (2001), p. 2834.

[43] d'Avezac, M. Calandra and F. Mauri: Phys. Rev. B Vol. 1 (2005), p. 205210.

[44] A. Droghetti, C. D. Pemmaraju and S. Sanvito: Phys. Rev. B Vol. 78 (2008), p. 140404.

[45] S. Elfimov, A. Rusydi, S. I. Csiszar, Z. Hu, H. H. Hsieh, H.J. Lin, C. T. Chen, R. Liang, and G. A. Sawatzky: Phys. Rev. Lett. Vol. 98 (2007), p. 137202.

[46] V. Pardo and W. E. Pickett: Phys. Rev. B Vol. 78 (2008), p. 134427.

[47] J. A. Chan, S. Lany and A. Zunger: Phys. Rev. Lett. Vol. 103 (2009), p. 016404.

[48] Y. Yan, M. M. Al-Jassim and S. H. Wei: Appl. Phys. Lett. Vol. 89 (2006), p. 181912.

[49] S. Lany and A. Zunger: Phys. Rev. B. Vol. 80 (2009), p. 085202.

[50] M. Venkatesan, C. B. Fitzgerald and J. M. D. Coey: Nature Vol. 430 (2004), p. 630.

[51] C. D. Pemmaraju and S. Sanvito: Phys. Rev. Lett. Vol. 94 (2005), p. 217205.

[52] L. A. Errico, M. Rentería, and M. Weissmann: Phys. Rev. B Vol. 72 (2005), p. 184425.

[53] N. H. Hong, J. Sakai, N. Poirot and V. Brizé: Phys. Rev. B Vol. 73 (2006), p. 132404.

[54] M. Weissmann and L. A. Errico: Physica B Vol. 398 (2007), p. 179.

[55] A. Sundaresan, R. Bhargavi, N. Rangarajan, U. Siddesh and C. N. R. Rao: Phys. Rev. B Vol. 74 (2006), p. 161306.

[56] N. H. Hong, A. Barla, J. Sakai and N. Q. Huong: Phys. Status Solidi C Vol. 4 (2007), p. 4461.

[57] H. Peng, H. J. Xiang, S. H. Wei, S. S. Li, J. B. Xia and J. Li: Phys. Rev. Lett. Vol. 102 (2009), p. 017201.

[58] N. H. Hong, N. Poirot and J. Sakai: Phys. Rev. B Vol. 77 (2008), p. 033205.

[59] S. Duhalde, M. F. Vignolo, F. Golmar, C. Chiliotte, C. E. Rodríguez Torres, L. A. Errico, A. F. Cabrera, M. Rentería, F. H. Sánchez, and M. Weissmann: Phys. Rev. B Vol. 72 (2005), p. R161313.

[60] H. S. Majumdar, S. Majumdar, D. Tobjörk and R. Österbacka: Synthetic metals (2009).

[61] H. Winkler and E. Gerdau: Z. Phys. Vol. 262 (1973), p. 363.

[62] N. Achtziger and W. Witthuhn: Phys. Rev. B Vol. 47 (1993), p. 6990.

[63] O. Keski-Rahkonen and M. O. Krause: Atomic Data Nucl. Data Tables 14 (1974), p. 139.

[64] A. Bartos, K. P. Lieb, A. F. Pasquevich, M. Uhrmacher and the ISOLDE collaboration: Phys. Lett. A Vol. 157 (1991), p. 513.

[65] D. Lupascu: program DYNXWW, program for calculating perturbation functions of fluctuating EFG's between arbitrary coordinate systems, contains the NAG© routines F01AMF, F01AVF,F01AWF, F02ARF, F04ADF.

[66] D. Lupascu, M. Neubauer, S. Habenicht, T. Wenzel, M. Uhrmacher, and K. P. Lieb, in: *Condensed Matter Studies by Nuclear Methods*, edited by K. Tomala and E. A. Görlich, p. 196, Institute of Physics, Krakow (1995).

[67] U. Bäverstam, R. Othaz, N. de Sousa and B. Ringstrom: Nuclear Physics Vol. A186 (1972), p. 500.

[68] A. Abragam and R. V. Pound: Phys. Rev. Vol. 92 (1953), p. 943.

[69] D. Dillenburg and Th. A. Maris: Nucl. Phys. Vol. 33 (1962), p. 208.

[70] H. Gabriel: Phys. Rev. Vol. 181 (1969), p. 506.

[71] M. Blume: *Hyperfine structure and nuclear radiations*, edited by E. Matthias and D. A. Shirley, North-Holland, Amsterdam (1968).

[72] M. Blume: Nucl. Phys. Vol. A167 (1971), p. 81.

[73] W. Sato, Y. Itsuki, S. Morimoto, H. Susuki, S. Nasu, A. Shinohara, and Y. Ohkubo: Phys. Rev. B Vol. 78 (2008), p. 045319.

[74] Ch. Y. Wang: Thin Solid Films Vol. 515 (2007), p. 6611.

[75] C. Falcony, J. R. Kirtley, D. J. Dimaria, T. P. Ma and T. C. Chen: J. Appl. Phys. Vol. 58 (1985), p. 3556.

[76] C. G. Granqvist: Appl. Phys, A Mater. Sci. Process. Vol. 57 (1993), p. 19.

[77] S. Kasiviswanathan and G. Rangarajan: J. Appl. Phys. Vol. 75 (1994), p. 2572.

[78] G. Kiriakidis, M. Bender, N. Katsarakis, E. Gagaoudakis, E. Hourdakis, E. Douloufakis and V. Cimalla: Phys. Status Solidi, A Appl. Res. Vol. 185 (2001), p. 27.

[79] D. H. Zhang, Z. Q. Liu and Ch. W. Zhou: Mater. Res. Soc. Symp. Proc. Vol. 828 (2005), p. A2.7.1

[80] ICDD PDF-2 Data base, JCPDS-Int. (Center for Diffraction Data, Pennsylvania, USA 1994).

[81] R. D. Shannon: Solid State Commun. Vol. 4 (1966), p. 629.

[82] A. Nørlund Christensen and N. C. Broch: Acta Chem. Scand. Vol. 21 (1967), p. 1046.

[83] T. J. Coutts, T. O. Mason, J. D. Perkins, and D. S. Ginley, in: *Transparent conducting oxides: status and opportunities in basic research*, p. 274, The Electrochemical Society, Inc. Seattle, Washington (1999).

[84] P. Lehmann and J. Miller: Le Journal de Physique et le Radium Vol. 17 (1956), p. 526.

[85] H. Frauenfelder: Proceedings of the meeting on *"Extranuclear Perturbations in Angular Correlations"*, edited by Karlsson, E. Mathias and K. Siegbahn, (Amsterdam) (1964), p. 329.

[86] A. Salomon: Nucl. Phys. Vol. 54 (1964), p. 171.

[87] M. Uhrmacher and W. Bolse: Hyperfine Interact. Vol. 15/16 (1983), p. 445.

[88] S. Habenicht, D. Lupascu, M. Uhrmacher, L. Ziegeler, K. P. Lieb and the ISOLDE Collaboration: Z. Phys. B Vol. 101 (1996), p. 187.

[89] A. Bartos, K. P. Lieb, M. Uhrmacher and D. Wiarda: Acta Cryst. B Vol. 49 (1993), p. 165.

[90] E. L. Muñoz, PhD Thesis, Departamento de Física, UNLP, to be defended March 2011.

[91] M. Rentería, F. G. Requejo, A. G. Bibiloni, A. F. Pasquevich, J. Shitu and K. Freitag: Phys. Rev. B Vol. 55 (1997), p. 14200.

[92] M. Rentería, K. Freitag and L. A. Errico: Hyperfine Interact. Vol. 120/121 (1999), p. 449.

[93] M. Rentería, A. G. Bibiloni, F. G. Requejo, A. F. Pasquevich, J. Shitu, L. A. Errico and K. Freitag: Mod. Phys. Lett. B Vol. 12 (1998), p. 819.

[94] A. F. Pasquevich, A. G. Bibiloni, C. P. Massolo, M. Rentería, J. A. Vercesi and K. Freitag: Phys. Rev. B Vol. 49 (1994), p. 14331.

[95] L. A. Errico, M. Rentería, A. F. Pasquevich, A. G. Bibiloni and K. Freitag: Eur. Phys. J. B Vol. 22 (2001), p. 149.

[96] E. L. Muñoz, G. N. Darriba, A. G. Bibiloni, L. A. Errico, and M. Rentería: J. of Alloys and Compounds Vol. 495 (2010), p. 532.

[97] M. Rentería, L. A. Errico and A. G. Bibiloni: "A First Principle Model For Electron-Capture After-Effects in ^{111}Cd: In_2O_3", Contribution to the Int. Workshop "At The Frontiers of Condensed Matter Physics III". 11-15 December 2006, Buenos Aires, Argentina. To be published.

[98] R. A. Quille, C. Y. Chain, L. C. Damonte, and A. F. Pasquevich: private communication.

[99] R. L. Weiher: J. Appl. Phys. Vol. 33 (1962), p. 2834.

[100] W. Bolse, M. Uhrmacher and J. Kesten: Hyperfine Interact 35 (1987) 931; W. Bolse, M. Uhrmacher, and K. P. Lieb: Phys. Rev. B Vol. 36 (1987), p. 1818.

[101] M. S. Moreno, J. Desimoni, F. G. Requejo, M. Rentería, A. G. Bibiloni and K. Freitag: Hyperfine Interact. Vol. 62 (1990), p. 353.

[102] M. S. Moreno, J. Desimoni, A. G. Bibiloni, M. Rentería, C. P. Massolo and K. Freitag: Phys. Rev. B Vol. 43 (1991), p. 10086.

[103] E. L. Muñoz, D. Richard, L. A. Errico, and M. Rentería: Physica B Vol. 404 (2009), p. 2757.

[104] Th. Wenzel, A. Bartos, K. P. Lieb, M. Uhrmacher, D. Wiarda: Ann. Phys. Vol. 1 (1992), p. 155.

[105] M. Rentería, A. G. Bibiloni, M. S. Moreno, J. Desimoni, R. C. Mercader, A. Bartos, M. Uhrmacher, and K. P. Lieb: J. Phys.: Condens. Matter Vol. 3 (1991), p. 3625.

[106] M. Neubauer, A. Bartos, K. P. Lieb, D. Lupascu, M. Uhrmacher and Th. Wenzel: Europhys. Lett. Vol. 29 (1995), p. 175.

[107] Fiorentini and G. Gulleri: Phys. Rev. Lett. Vol. 89 (2002), p. 266101

[108] A. S. Foster, F. Lopez Gejo, A. L. Shluger and R. M. Nieminen: Phys. Rev. B Vol. 65 (2002), p. 174117.

[109] J. Kang, E. C. Lee and K. J. Chang: Phys. Rev. B Vol. 68 (2003), p. 54106.

[110] J. E. Jaffe, R. A. Bachorz and M. Gutowski: Phys. Rev. B Vol. 72 (2005), p. 144107.

[111] A. B. Mukhopadhyay, J. F. Sanz and C. B. Musgrave: Phys. Rev. B Vol. 73 (2006), p. 115330.

[112] J. M. D. Coey, M. Venkatesan, P. Stamenov, C. B. Fitzgerald and L. S. Dorneles: Phys. Rev. B Vol. 72 (2005), p. 024450.

[113] N. Hadacek, A. Nosov, L. Ranno, P. Strobel and R. M. Galéra: J. Phys.: Condens. Matter Vol. 19 (2007), p. 486206.

[114] Y. Yeshurun and B. Arad: J. Phys. Vol. 7 (1974), p. 430.

[115] H. Barfuss, G. Böhnlein, H. Hohenstein, W. Kreische, H. Niedrig, H. Appel, R. Heidinger, J. Raudies, G. Then, and W.-G. Thies: Z. Phys. B Vol. 47 (1982), p. 99.

[116] A. Baudry, P. Boyer, and P. Vulliet: Hyperfine Interact. Vol. 13, (1983), p. 263.

[117] S. Koicki, M. Manasijevic, and B. Cekic: Hyperfine Interact. Vol. 14 (1983), p. 105.

[118] H. Jaeger, J.A. Gardner, J.C. Haygarth and R. L. Rasera: J. Am. Ceram. Soc. Vol. 69 (1986), p. 458.

[119] M. C. Caracoche, J. A. Martinez, P. C. Rivas, and A. Lopez- Garcia: Hyperfine Interact. Vol. 39 (1988), p. 117.

[120] A. Ayala, R. Alonso and A. López-Garcia: Phys. Rev. B Vol. 50 (1994), p. 3547.

[121] A. F. Pasquevich, F. H. M. Cavalcante and J. C. Soares: Hyperfine Interact Vol. 179 (2007), p. 67.

[122] R. A. Quille and A. F. Pasquevich: Journal of Alloys and Compounds Vol. 495 (2009), p. 634.

[123] M. Forker, P. de la Presa, W. Hoffbauer, S. Schlabach, M. Bruns and D. V. Szabó: Phys. Rev. B Vol. 77 (2008), p. 54108.

[124] A. Baudry and P. Boyer: Hyperfine Interact. Vol. 35 (1987), p. 803.

[125] S. Schlabach, D. V. Szabó, D. Vollath, P. de la Presa and M. Forker: J. Appl. Phys. Vol. 100 (2006), p. 024305.

[126] M. Forker, U. Brossmann, and R. Würschum: Phys. Rev. B Vol. 57 (1998), p. 5177.

[127] J. Luthin, K. P. Lieb, M. Neubauer, M. Uhrmacher and B. Lindgren: Phys. Rev. B Vol. 57 (1998), p. 15272.

[128] U. Brossmann, R. Würschum, U. Södervall, and H.-E. Schaefer: J. Appl. Phys. Vol. 85 (1999), p. 764

[129] P. Heitjans and S. Indris: J. Phys.: Condens. Matter Vol. 15(2003), p. R1257.

[130] R. A. Casali and M. A. Caravaca: Solid State Commun. Vol. 134 (2005), p. 413.

[131] R. E. Alonso, L. A. Errico, E. L. Peltzer y Blancá, A. López-García, A. Svane, and N. E. Christensen: Phys. Rev. B Vol. 78 (2008), p. 165206.

[132] S. Shukla and S. Seal: Int. Mater. Rev. Vol. 50 (2005), p. 4.

[133] J. Kang, E.-C. Lee, K. J. Chang, and Y. G. Jin: Appl. Phys. Lett. Vol. 84 (2004), p. 3894 .

[134] D. Lupascu, J. Albohn, J. Shitu, A. Bartos, K. Królas, M. Uhrmacher, and K. P. Lieb: Hyperfine Interact. Vol. 80 (1993), p. 959.

[135] S. Habenicht, D. Lupascu, M. Neubauer, M. Uhrmacher, K. P. Lieb, and the ISOLDE collaboration: Hyperfine Interact. Vol. 120/121 (1999), p. 445.

[136] J. Kesten, M. Uhrmacher, and K. P. Lieb: Hyperfine Interact. Vol. 59 (1990), p. 309.

[137] K. Asai, F. Ambe, S. Ambe, T. Okada, and H. Sekizawa: Phys. Rev. B Vol. 41 (1990), p. 6124.

[138] J. Kesten, W. Bolse, K. P. Lieb, M. Uhrmacher: Hyperfine Interact. Vol. 60 (1990), p. 683.

[139] M. Forker, H. Saitovitch, and P. R. de Jesus Silva: J.Phys. C: Solid State Phys. Vol. 17 (1984), p. 1055.

[140] D. Wiarda, T. Wenzel, M. Uhrmacher, and K. P. Lieb: J. Phys. Chem. Solids Vol. 53 (1992), p. 1199.

[141] A. W. Carbonari, J. Mestnik-Filho, R. N. Attili, M. Morales, and R. N. Saxena: Hyperfine Interact. Vol. 120/121 (1999), p. 475.

[142] A. F. Pasquevich, A. M. Rodriguez, H. Saitovitch, and P. R. de Jesus Silva: contribution to the 77° Argentinian Physics Association Conference, Bs. As, 1992, private communication.

[143] J. Shitu, D. Wiarda, T. Wenzel, M. Uhrmacher, K. P. Lieb, S. Bedi, and A. Bartos: Phys. Rev. B Vol. 46 (1992), p. 7987.

[144] J. Desimoni, A. G. Bibiloni, C. P. Massolo and M. Rentería: Phys. Rev. B. Vol. 41(1990), p. 1443.

[145] W. Bolse, M. Uhrmacher, and K. P. Lieb: Hyperfine Interact. Vol. 35 (1987), p. 631.

[146] M. Rentería, D. Wiarda, A. G. Bibiloni, and K. P. Lieb: Hyperfine Interact. Vol. 60 (1990), p. 679.

[147] M. Rentería: Ph.D. Thesis, University of La Plata (UNLP), 1992.

[148] F. G. Requejo, A .G. Bibiloni, C. P. Massolo, J. Desimoni, and M. Rentería: Phys. Stat. Solidi (a) Vol. 116 (1989), p. 503.

[149] D. Wegner, Z. Inglot, and K. P. Lieb: Ber. Bunsengs. Phys. Chem. Vol. 94 (1990), p. 1.

[150] M. E. Mercurio, A. W. Carbonari, M. R. Cordeiro, and R. N. Saxena: Hyperfine Interact. Vol. 178 (2007), p. 247.

[151] A. Bartos, W. Bolse, K. P. Lieb, and M. Uhrmacher: Phys. Lett. A Vol. 130 (1988), p. 177.

[152] C. P. Massolo, M. Rentería, J. Desimoni, and A. G. Bibiloni: Phys. Rev. B Vol. 37 (1988), p. 4743.

[153] D. Lupascu , M. Uhrmacher, and K. P. Lieb: J. Phys.: Condens. Matter Vol. 6 (1994), p. 10445.

[154] M. Rentería, L. A. Errico, A .G. Bibiloni, F. G. Requejo, and K. Freitag: Z. für Naturforschung A Vol. 55 (2000), p. 155

[155] M. Rentería, G. N. Darriba, L. A. Errico, E. L. Muñoz, and P. D. Eversheim: Phys. Stat. Solidi B Vol. 242 (2005), p. 1928.

[156] A. F. Pasquevich, A. C. Junqueira, A. W. Carbonari, and R. N. Saxena: Hyperfine Interact. Vol. 158 (2004), p. 371.

[157] G. N. Darriba, E. L. Muñoz, P. D. Eversheim, and M. Rentería: Hyperfine Interact. (in press 2010).

[158] J. Shitu and A. F. Pasquevich: J. Phys.: Condensed Matt. Vol. 9 (1997), p. 6313.

[159] E. L. Muñoz, D. Richard, P. D. Eversheim, and M. Rentería: Hyperfine Interact. (in press 2010).

[160] M. C. Caracoche, J. A. Martinez, P. C. Rivas, A. R. López-García: Hyperfine Interact. Vol. 23 (1985), p. 221.

[161] M. Rentería, L. A. Errico, A. G. Bibiloni, and K. Freitag: to be published.